Modelling the particle trajectory and melting behaviour of non-spherical ice crystal particles

Xin Yang*, Matthew McGilvray, David R.H. Gillespie

Department of Engineering Science, Oxford Thermofluids Institute,University of Oxford, Oxford OX2 0ES, UK

Abstract

Existing ice crystal icing codes commonly neglect non-spherical particle rotation behaviour. This leads to uncertainties in modelling ice crystal icing as ice crystals are typically non-spherical. This paper develops a two-dimensional framework to model the particle trajectory and melting behaviour of rotating non-spherical ice crystal particles. Non-spherical particle translational and rotational motions are resolved using a framework of unit complex numbers. The effect of rotation on particle heat and mass transfer is implemented using a sub-model dependent on both rotational and translational particle Reynolds numbers. A test case of flow through a swan neck duct is presented. The model is validated through comparison to the discrete phase model in ANSYS Fluent and experimental water droplet impingement test data. Comparison of the developed framework with other simplified particle tracking methods (without modelling the non-spherical particle rotation) is first conducted. These results show large differences in the trajectory, velocity and melt ratio of individual particles and in overall particle impingement behaviours, especially for high aspect ratio particles. Particle rotation can indirectly affect single particle's melting behaviour through its effect on particle trajectory and velocity. Both aspect ratio and porosity are seen to enhance particle melting behaviour and affect particle impingement behaviour. The numerical uncertainties in the DNS-based correlations of the particle forces and torques employed are also discussed, as well as the performance of the developed framework for the case of a flow past a test article.

Keywords: Ice crystal icing, Non-spherical particles, Particle tracking, Particle melting

1. Introduction

Ice crystal icing (ICI) has been identified as a serious threat to jet engines. Several engine power-loss and damage events have been caused possibly by ice crystal icing (Mason et al., 2006). Ice particles in clouds can be found at high altitude (above 7000 m) near the deep convective clouds in tropical regions, having a median mass diameter of 60 μm-100 μm with irregular particle shapes (Mason et al., 2011). After ingestion into an engine, ice particles may fragment into smaller particles due to impingement on the engine fans/vanes. Then, ice particles will partially melt due to the heat transfer with the warm airflow or impingement on the warm

*Corresponding author
Email address: xin.yang@eng.ox.ac.uk (Xin Yang)

surfaces inside the engine compressor. Partially / fully melted ice particles can stick onto the surfaces inside the engine, creating a water film at the warm surfaces and building ice accretion on the water film. Serious ice accretions can cause the flow blockage, which will result in an engine malfunction (surge, stall, flameout and rollback, as well as compressor damages) (Mason et al., 2006).

Several icing codes for glaciated and mixed phase conditions have been developed in order to support the preliminary design and certification of de-icing systems. Wright et al. (2010, 2015) adapted NASA Glenn's icing codes, GlennICE and LEWICE, to ICI via modifying the models of particle drag force, particle heat and mass transfer, and accretion surface energy balance. A similar adaptation of TAICE can also be found by Ayan and Özgen (2018). Villedieu et al. (2014) developed an ice accretion code (IGLOO2D) for mixed-phase and glaciated icing conditions. Correlations of Nusselt number and Sherwood number for non-spherical particles have been derived to predict the melting behaviour of ice particles. IGLOO2D uses a threshold (the ratio of particle normal kinetic energy to particle surface energy) to determine impact outcomes (sticking, bouncing and shattering regimes). Furthermore, particle sticking and erosion models are developed in IGLOO2D in order to determine the sticking efficiency and erosion efficiency (Trontin and Villedieu, 2018). In addition to Lagrangian based icing codes, an extension of Euler based icing codes to ICI is found in Norde et al. (2017, 2019) and Nilamdeen et al. (2019). Recently, Bucknell et al. (2019c,a) developed a glaciated and mixed phase icing code (ICICLE), which adopted a framework similar to existing Lagrangian based codes with improved ICI modelling through (i) experimentally-derived sticking and erosion models and (ii) adapting the Extended Messinger Model (EMM) for the mixed phase conditions on the warm surfaces.

These icing codes have made significant progress in modelling ICI. However, in the existing icing codes, the non-spherical particle rotational motion is commonly neglected. Particle rotation affects (i) drag and lift forces, and thus particle trajectory, (ii) particle heat and mass transfer, which affects particle melting behaviour, (iii) particle-wall interaction. Widhalm (2015) developed a Lagrangian framework which combines the particle translational and rotational motions and investigated the effect of particle shape (cylinders and disks) on the collection efficiency. The results show that particle rotation can affect the collection efficiency in flow with strong flow acceleration or deceleration. Recently, Palmer et al. (2019) also developed a similar Lagrangian framework for the non-spherical particle tracking, based on previous work by van Wachem et al. (2015). However, the value of these cited studies is limited by modelling particle tracking without considering the particle phase change behaviour. Therefore, the effect of non-spherical particle rotation on the melting behaviour of ice particles is still unclear. Moreover, little work has been published comparing rotational and simplified non-rotational particle tracking methods. This is essential to understand the performance of these methods and the validity of using the simplified methods for modelling non-spherical particle behaviours.

This paper aims to investigate the effect of non-spherical particle rotation on both particle trajectory and melting behaviour, and to understand the validity of the use of simplified particle tracking methods for modelling ICI. A new two-dimensional non-spherical particle tracking framework integrated with particle phase change models has been developed and incorporated in the in-house icing code, ICICLE. The developed

framework in this paper is firstly validated against the discrete phase model in the commercial CFD software, ANSYS Fluent, and additionally using experimental data from water droplet impingement test. This framework is then used to model the particle trajectory and melting behaviour of non-spherical ice crystal particles. The prediction results are compared with those predicted using simplified particle tracking methods (including spherical particle tracking without rotation, non-spherical particle tracking without rotation, and spherical particle tracking with rotation), which are used in various icing codes. The ranges of particle-flow conditions investigated are chosen to match icing tests carried out at the RATFac icing wind tunnel of NRC. These are also typical downstream of the fan in a large civil turbofan engine. The flow geometry modelled in this study is representative of a compressor swan neck duct.

2. Mathematical models

In order to model non-spherical particle rotation for ice crystal accretion, efforts have been made to produce an accurate numerical description of the dynamics of non-spherical particles, particle phase change modelling, and particle wall interaction. To achieve this, a two dimensional framework, which is detailed in this section, has been developed and several submodels applied.

2.1. Dynamics of non-spherical particles.

Particle motions consist of translational and rotational components. Modelling the particle motions of non-spherical particles are more complicated than that of spherical particles due to the particle orientation. In order to conveniently solve the particle rotational motion of non-spherical particles, two types of Cartesian co-ordinate systems are required: body space (in reference to particles, x^B, y^B, z^B) and global space (x^G, y^G, z^G). Particle translational motion is derived in the global space while particle rotational motion is derived in the body space. The mapping of parameters (velocities, forces, etc.) between the body and global spaces in three-dimensional (3D) space is often done by using a unit Quaternion, which is composed of the rotation axis and angle (Widhalm, 2015; van Wachem et al., 2015; Palmer et al., 2019). In this study, the developed framework of particle motion equations is kept two-dimensional (2D) in order to reduce the computational cost. In this framework the unit Quaternion is reduced to a unit complex number. In 2D particle tracking, the rotation of non-spherical particles is around the z axis since particles are fixed in the x-y plane. Therefore, the Cartesian co-ordinate systems can be simplified in the body space (x^B, y^B, z) and the global space (x^G, y^G, z) in which z is used to represent the rotation axis, as shown in Fig.1.

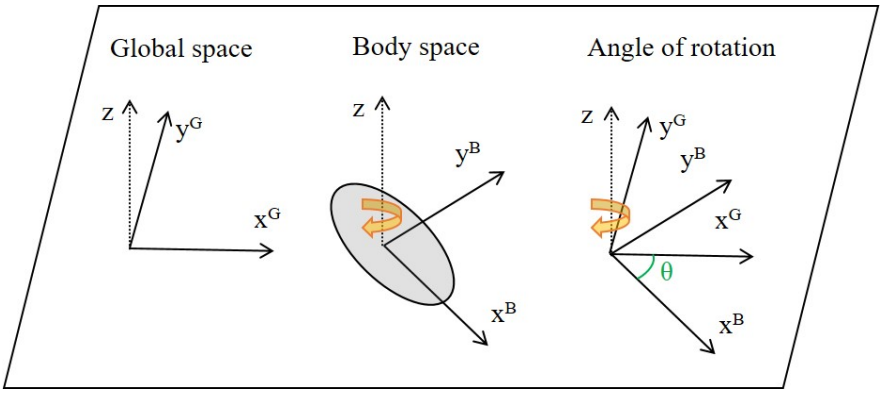

Figure 1: The two Cartesian co-ordinate systems and the angle of rotation, θ, between the two co-ordinates.

2.1.1. Rotation by unit complex number

Manipulation of particle rotation in the 2D plane is done using unit complex numbers, c. The manipulation is divided into three types, (i) rotation within the same Cartesian co-ordinate system, (ii) rotation from the global space to the body space, and (iii) rotation from the body space to the global space. The manipulation of type (i) in the global space is mathematically equivalent to type (iii). These manipulations, which are key to mapping flow and force parameters (velocities, forces, etc.) between the body and global spaces, are defined by:

$$\overrightarrow{x}' = \begin{cases} \overrightarrow{x}\overrightarrow{c_1} & \text{type (i) and (iii)} \\ \overrightarrow{x}\overrightarrow{c_2} & \text{type (ii)} \end{cases} \tag{1}$$

$$\overrightarrow{c_1} = [\cos(\theta), \mathbf{i}\sin(\theta)] \tag{2}$$

$$\overrightarrow{c_2} = [\cos(\theta), -\mathbf{i}\sin(\theta)] \tag{3}$$

where, $\overrightarrow{x}$ and $\overrightarrow{x}'$ are the vectors before and after the manipulation of rotation, respectively.

2.1.2. Translational motion

The translational motion equations of non-spherical particles are similar to spherical particles, which are governed by the force balance equations:

$$\frac{\mathrm{d}\overrightarrow{X_\mathrm{p}^\mathrm{G}}}{\mathrm{d}t} = \overrightarrow{v_\mathrm{p}^\mathrm{G}} \tag{4}$$

$$m_\mathrm{p}\frac{\mathrm{d}\overrightarrow{v_\mathrm{p}^\mathrm{G}}}{\mathrm{d}t} = \overrightarrow{F_\mathrm{D}^\mathrm{G}} + \overrightarrow{F^\mathrm{G}} \tag{5}$$

where, $\overrightarrow{X_\mathrm{p}^\mathrm{G}}$ is the particle location, $\overrightarrow{v_\mathrm{p}^\mathrm{G}}$ and m are the particle velocity and mass, respectively; $\overrightarrow{F_\mathrm{D}^\mathrm{G}}$ is the drag force; $\overrightarrow{F^\mathrm{G}}$ are other forces, including lift forces, gravity, virtual mass force, pressure gradient force, thermophoretic force, etc. Virtual mass and pressure gradient forces are neglected due to the particle density being much larger than the gas density; thermophoretic force is neglected due to the small temperature

gradient; Saffman's lift force is neglected since the force is for sub-micron particles. Therefore, in addition to drag force, only aerodynamic lift force ($\overrightarrow{F_{\rm la}^{\rm G}}$) and Magnus lift force (rotational lift force, $\overrightarrow{F_{\rm lr}^{\rm G}}$) are included in this study.

Drag force, $\overrightarrow{F_{\rm D}^{\rm G}}$, acts in the opposite direction of the relative motion of particles with respect to the fluid flow and is written as:

$$\overrightarrow{F_{\rm D}^{\rm G}} = \frac{1}{8}\rho_{\rm g}{\rm C_D}\pi D_{\rm p}^2\left|\overrightarrow{v_{\rm g}^{\rm G}}-\overrightarrow{v_{\rm p}^{\rm G}}\right|(\overrightarrow{v_{\rm g}^{\rm G}}-\overrightarrow{v_{\rm p}^{\rm G}}) \tag{6}$$

where, $\overrightarrow{v^{\rm G}}$, ρ, m, and $D_{\rm p}$ are the velocity, density, mass, and diameter, respectively; the subscripts p and g refer to the particle and gas, respectively, $\rm C_D$ is the drag coefficient. Several expressions are found for the correlations of $\rm C_D$ of non-spherical particles as a function of particle Reynolds number ($\mathrm{Re_p}=\rho_{\rm g}\left|\overrightarrow{v_{\rm g}^{\rm G}}-\overrightarrow{v_{\rm p}^{\rm G}}\right|D_{\rm p}/\mu_{\rm g}$), particle shape (aspect ratio, AR, or sphericity, $\Phi=\pi D_{\rm p}^2/A_{\rm p}$) and particle orientation (incidence angle, φ, defined as the angle between the direction of the gas velocity in the body space and the long axis of the particle (van Wachem et al., 2015), or crosswise sphericity, $\Phi_\perp=\pi D_{\rm p}^2/(4A_{\rm p,\perp})$). Hölzer and Sommerfeld (2008) proposed a general correlation of drag coefficient as a function of $\mathrm{Re_p}$, Φ, and $\Phi_\perp$. It is clarimed that this general correlation is valid for all particle shapes. However, the use of Φ alone can not fully describe particle shape. Zastawny et al. (2012) derived an expression for drag coefficient as a function of $\mathrm{Re_p}$, φ, and AR using direct numerical simulation (DNS). However, here only prolate particles of aspect ratios 1.25 and 2.5 were considered. Later, Ouchene et al. (2016) derived a correlation for the drag coefficient of prolate particles with aspect ratio ranging from 1.25 to 32 from DNS simulations. Therefore, their correlation using the typographically corrected coefficient constants in Arcen et al. (2017), which is valid for $\mathrm{Re_p}$<240, is adopted in this study and the drag coefficient is predicted by:

$$\mathrm{C_D} = \mathrm{C_{D,0}}+(\mathrm{C_{D,\pi/2}}-\mathrm{C_{D,0}})\sin^2(\varphi) \tag{7}$$

$$\mathrm{C_{D,0}} = \frac{24}{\mathrm{Re_p}}\left[\mathrm{K_0(AR)}+0.15\mathrm{AR}^{-0.8}\mathrm{Re_p}^{0.687}+\frac{(\mathrm{AR}-1)^{0.63}\mathrm{Re_p}^{0.41}}{24}\right] \tag{8}$$

$$\mathrm{C_{D,\pi/2}} = \frac{24}{\mathrm{Re_p}}\left[\mathrm{K_{\pi/2}(AR)}+0.15\mathrm{AR}^{-0.54}\mathrm{Re_p}^{0.687}+\frac{\mathrm{AR}^{1.043}(\mathrm{AR}-1)^{-0.17}\mathrm{Re_p}^{0.65}}{24}\right] \tag{9}$$

$$\mathrm{K_0(AR)} = \frac{8}{3}\mathrm{AR}^{\frac{-1}{3}}\left[\frac{-2\mathrm{AR}}{\mathrm{AR}^2-1}+\frac{2\mathrm{AR}^2-1}{(\mathrm{AR}^2-1)^{3/2}}\ln\left(\frac{\mathrm{AR}+\sqrt{\mathrm{AR}^2-1}}{\mathrm{AR}-\sqrt{\mathrm{AR}^2-1}}\right)\right]^{-1} \tag{10}$$

$$\mathrm{K_{\pi/2}(AR)} = \frac{8}{3}\mathrm{AR}^{\frac{-1}{3}}\left[\frac{\mathrm{AR}}{\mathrm{AR}^2-1}+\frac{2\mathrm{AR}^2-3}{(\mathrm{AR}^2-1)^{3/2}}\ln\left(\mathrm{AR}+\sqrt{\mathrm{AR}^2-1}\right)\right]^{-1} \tag{11}$$

$$\varphi = \arctan\left(\frac{\mathrm{v_{g,y}^B}}{\mathrm{v_{g,x}^B}}\right) \tag{12}$$

Aerodynamic lift force, $\overrightarrow{F_{\rm la}^{\rm G}}$, acts in the direction perpendicular to the flow direction and is written as

(van Wachem et al., 2015; Palmer et al., 2019):

$$\overrightarrow{F_{\mathrm{la}}^{\mathrm{G}}} = \overrightarrow{F_{\mathrm{la}}^{\mathrm{B}}}\overrightarrow{c_1} \tag{13}$$

$$\overrightarrow{F_{\mathrm{la}}^{\mathrm{B}}} = \frac{1}{2}\rho_{\mathrm{g}}\mathrm{C_{la}}A_{\mathrm{p}}\left|\overrightarrow{v_{\mathrm{g}}^{\mathrm{B}}} - \overrightarrow{v_{\mathrm{p}}^{\mathrm{B}}}\right|^2 \overrightarrow{\mathrm{L}^{\mathrm{B}}} \tag{14}$$

$$\overrightarrow{\mathrm{L}^{\mathrm{B}}} = \begin{cases} \sin(\varphi)sign(-(v_{\mathrm{g,x}}^{\mathrm{B}} - v_{\mathrm{p,x}}^{\mathrm{B}})) & \text{x direction} \\ \cos(\varphi)sign((v_{\mathrm{g,y}}^{\mathrm{B}} - v_{\mathrm{p,y}}^{\mathrm{B}})) & \text{y direction} \end{cases} \tag{15}$$

where, A_{p} is the particle area; C_{la} is the aerodynamic lift coefficient, which is predicted by Ouchene et al. (2016):

$$\mathrm{C_{la}} = \left[\mathrm{F_L(AR)Re_p^{0.25}} + \frac{\mathrm{G_L(AR)}}{\mathrm{Re_p^{0.755}}}\right]\cos(\varphi)\sin^{1.002^{\mathrm{Re_p}}}(\varphi) \tag{16}$$

$$\mathrm{F_L(AR)} = 0.1944(\mathrm{AR}^{-0.93} - 1)\ln(\mathrm{AR}) + 0.2127(\mathrm{AR} - 1)^{0.47} \tag{17}$$

$$\mathrm{G_L(AR)} = 0.9183(\mathrm{AR} - 1)^{0.46}\ln(\mathrm{AR}) - 4.0573(\mathrm{AR}^{-1.61} - 1) \tag{18}$$

Magnus lift force, $\overrightarrow{F_{\mathrm{lr}}^{\mathrm{G}}}$, is caused by the pressure differential along the surface of rotating particles and is predicted by:

$$\overrightarrow{F_{\mathrm{lr}}^{\mathrm{G}}} = \overrightarrow{F_{\mathrm{lr}}^{\mathrm{B}}}\overrightarrow{c_1} \tag{19}$$

$$\overrightarrow{F_{\mathrm{lr}}^{\mathrm{B}}} = \frac{1}{2}\rho_{\mathrm{g}}\mathrm{C_{lr}}A_{\mathrm{p}}\frac{|\overrightarrow{v_{\mathrm{g}}^{\mathrm{B}}} - \overrightarrow{v_{\mathrm{p}}^{\mathrm{B}}}|}{|\overrightarrow{\omega_{\mathrm{g}}} - \overrightarrow{\omega_{\mathrm{p}}}|}((\overrightarrow{v_{\mathrm{g}}^{\mathrm{B}}} - \overrightarrow{v_{\mathrm{p}}^{\mathrm{B}}}) \times (\overrightarrow{\omega_{\mathrm{g}}} - \overrightarrow{\omega_{\mathrm{p}}})) \tag{20}$$

where, $\mathrm{C_{lr}}$ is the Magnus lift coefficient and ω is the angular velocity. Due to the limited availability of correlations of $\mathrm{C_{lr}}$ for non-spherical particles, the correlation for spherical particles by Oesterlé and Dinh (1998), which is valid for $\mathrm{Re_p}$<2000 (Ansys Inc., 2018), is employed in this study:

$$\mathrm{C_{lr}} = 0.45 + \left(\frac{\mathrm{Re_\omega}}{\mathrm{Re_p}} - 0.45\right)\mathrm{e}^{-0.05684\mathrm{Re_\omega^{0.4}Re_p^{0.3}}} \tag{21}$$

where, the particle rotational Reynolds number, $\mathrm{Re_\omega}$=$\rho_{\mathrm{g}}|\overrightarrow{\omega_g} - \overrightarrow{\omega_p}|\mathrm{D_p^2}/\mu_{\mathrm{g}}$.

2.1.3. Rotational motion

The rotational motion equations of the non-spherical particles are governed by the angular momentum. For 2D planar rotation, the rotation axis is fixed at z and therefore, the rotational motion equations are written as:

$$\frac{\mathrm{d}\theta_{\mathrm{p,z}}}{dt} = \omega_{\mathrm{p,z}} \tag{22}$$

$$I_{\mathrm{p,z}}\frac{\mathrm{d}\omega_{\mathrm{p,z}}}{\mathrm{d}t} = T_{\mathrm{P,z}} + T_{\mathrm{R,z}} \tag{23}$$

where, $\theta_{\mathrm{p,z}}$ is the angle of rotation around z axis, $\omega_{\mathrm{p,z}}$ is the angular velocity of particles; the moment of inertia of prolate spheroid, $I_{\mathrm{p,z}} = \frac{m_{\mathrm{p}}}{20}\left[(\frac{d_{\mathrm{p,c}}}{\mathrm{AR}})^2 + d_{\mathrm{p,c}}^2\right]$, and $d_{\mathrm{p,c}}$ is the symmetry axis of the prolate particle; $T_{\mathrm{P,z}}$ and $T_{\mathrm{R,z}}$ are the pitching torque and rotational torque, respectively.

The pitching torque, $T_{\mathrm{P,z}}$, acts on the particles when the position of center of pressure of the particles does not coincide with the center of mass of the particles. This is caused by the incidence angle between the gas velocity vector and the principle axis of particles (van Wachem et al., 2015). The pitching torque, $T_{\mathrm{P,z}}$, is written as:

$$T_{\mathrm{P,z}} = \frac{1}{4}\rho_{\mathrm{g}}\mathrm{C_{TP}}A_{\mathrm{p}}D_{\mathrm{p}}\left|\overrightarrow{v_{\mathrm{g}}^{\mathrm{B}}}-\overrightarrow{v_{\mathrm{p}}^{\mathrm{B}}}\right| sign((v_{\mathrm{g,x}}^{\mathrm{B}}-v_{\mathrm{p,x}}^{\mathrm{B}})(v_{\mathrm{g,y}}^{\mathrm{B}}-v_{\mathrm{p,y}}^{\mathrm{B}})) \tag{24}$$

where, $\mathrm{C_{TP}}$ is the pitching torque coefficient, D_{p} is the volume equivalent particle diameter, and *sign* is the Signum function. The correlation for $\mathrm{C_{TP}}$ by Ouchene et al. (2016) is employed in this study. The correlation is given by:

$$\mathrm{C_{TP}} = \begin{cases} \ln(\mathrm{AR})\left[\frac{\mathrm{F_T(AR)}}{\mathrm{Re_p^{0.18}}}+\frac{\mathrm{G_T(AR)}}{\mathrm{Re_p^{0.51}}}\right]\cos^{0.9994^{\mathrm{Re_p}}}(\varphi)\sin(\varphi) & \mathrm{AR}\in[1,10] \\ \left[\frac{\mathrm{F_T(AR)}}{\mathrm{Re_p^{0.3}}}+\frac{\mathrm{G_T(AR)}}{\mathrm{Re_p^{0.9}}}\right]\cos^{0.9989^{\mathrm{Re_p}}}(\varphi)\sin(\varphi) & \mathrm{AR}\in[10,32] \end{cases} \tag{25}$$

$$\mathrm{F_T(AR)} = \begin{cases} 6.46(\mathrm{AR}^{-0.2212}-0.4855) & \mathrm{AR}\in[1,10] \\ 1.67\ln(\mathrm{AR})(\mathrm{AR}-1)^{0.24} & \mathrm{AR}\in[10,32] \end{cases} \tag{26}$$

$$\mathrm{G_T(AR)} = \begin{cases} 0.072(\mathrm{AR}-1)^{1.85} & \mathrm{AR}\in[1,10] \\ -2.71\ln(\mathrm{AR})+0.28\left((\mathrm{AR}^{1.65}-1)+(\mathrm{AR}-1)^{-0.22}\right) & \mathrm{AR}\in[10,32] \end{cases} \tag{27}$$

The rotational torque, $T_{\mathrm{R,z}}$, acts on a particle to counteract the particle rotation relative to the surrounding fluid and is proportional to the relative angular velocity. It is given by:

$$T_{\mathrm{R,z}} = \frac{1}{2}\rho_{\mathrm{g}}\mathrm{C_{TR}}\left(\frac{D_{\mathrm{p}}}{2}\right)^5|\overrightarrow{\omega_{\mathrm{g}}}-\overrightarrow{\omega_{\mathrm{p}}}|\,(\overrightarrow{\omega_{\mathrm{g}}}-\overrightarrow{\omega_{\mathrm{p}}}) \tag{28}$$

where, $\mathrm{C_{TR}}$ is the rotational torque coefficient. Due to the limited availability of the correlations of $\mathrm{C_{TR}}$ for the non-spherical particles, the correlation for spherical particles by (Dennis et al., 1980), which is valid for $\mathrm{Re_\omega}$<4000, is used. The formula is given by:

$$\mathrm{C_{TR}} = \mathrm{C_{Ra}}\left(\frac{\mathrm{Re_\omega}}{4}\right)^{-1/2}+\mathrm{C_{Rb}}\left(\frac{\mathrm{Re_\omega}}{4}\right)^{-1} \tag{29}$$

$$(\mathrm{C_{Ra}},\mathrm{C_{Rb}}) = \begin{cases} (5.32,37.2) & \mathrm{Re_\omega}<80 \\ (6.44,32.2) & \mathrm{Re_\omega}\in[80,200] \\ (6.45,32.1) & \mathrm{Re_\omega}\in[200,4000] \end{cases} \tag{30}$$

2.1.4. Integration of motion equations

The time integration strategy is important for the computational accuracy and stability, as well as the required simulation time. Both the translational and rotational motion equations consist of a set of coupled ordinary differential equations. Therefore, the motion equations are cast into the following general forms:

$$\frac{\mathrm{d}\psi}{\mathrm{d}t} = \nu \tag{31}$$

$$\frac{\mathrm{d}\nu}{\mathrm{d}t} = J_{\mathrm{a}}\nu+J_{\mathrm{b}} \tag{32}$$

where, ψ represents $\overrightarrow{X_{\mathrm{p}}^{\mathrm{G}}}$ and $\theta_{\mathrm{p,z}}$ for translational and rotational motions, respectively; ν represents $\overrightarrow{v_{\mathrm{p}}^{\mathrm{G}}}$ and $\omega_{\mathrm{p,z}}$, respectively. J_{a} and J_{b} are the corresponding coefficients in the motion equations and these may be written as:

$$J_{\mathrm{a,transl}} = -\frac{1}{2m_{\mathrm{p}}}\rho_{\mathrm{g}}\mathrm{C_D}A_{\mathrm{p},\perp}\left|\overrightarrow{v_{\mathrm{g}}^{\mathrm{G}}}-\overrightarrow{v_{\mathrm{p}}^{\mathrm{G}}}\right| \tag{33}$$

$$J_{\mathrm{b,transl}} = \frac{\overrightarrow{F_{\mathrm{la}}^{\mathrm{G}}}+\overrightarrow{F_{\mathrm{lr}}^{\mathrm{G}}}}{m_{\mathrm{p}}}+\frac{1}{2m_{\mathrm{p}}}\rho_{\mathrm{g}}\mathrm{C_D}A_{\mathrm{p},\perp}\left|\overrightarrow{v_{\mathrm{g}}^{\mathrm{G}}}-\overrightarrow{v_{\mathrm{p}}^{\mathrm{G}}}\right|\overrightarrow{v_{\mathrm{g}}^{\mathrm{G}}} \tag{34}$$

$$J_{\mathrm{a,rot}} = \frac{1}{2I_{\mathrm{p,z}}}\rho_{\mathrm{g}}\mathrm{C_{TR}}\left(\frac{D_{\mathrm{p}}}{2}\right)^5|\overrightarrow{\omega_{\mathrm{g}}}-\overrightarrow{\omega_{p}}| \tag{35}$$

$$J_{\mathrm{b,rot}} = \frac{1}{I_{\mathrm{p,z}}}\left[T_{\mathrm{P,z}}+\frac{1}{2}\rho_{\mathrm{g}}\mathrm{C_{TR}}\left(\frac{D_{\mathrm{p}}}{2}\right)^5|\overrightarrow{\omega_{\mathrm{g}}}-\overrightarrow{\omega_{\mathrm{p}}}|\,\overrightarrow{\omega_{\mathrm{g}}}\right] \tag{36}$$

where, the subscripts transl and rot represent the translational and rotational motions, respectively. The translational and rotational motion equations can be conveniently integrated via these general forms. In this study, the analytic discretization method is employed due to its stability and accuracy advantages. Therefore, the integrated forms of the general forms of motion equations are:

$$\nu^{\mathrm{n+1}} = e^{J_{\mathrm{a}}^{\mathrm{n}}\Delta t^{\mathrm{n}}}\nu^{\mathrm{n}}+\frac{J_{\mathrm{b}}^{\mathrm{n}}}{J_{\mathrm{a}}^{\mathrm{n}}}(e^{J_{\mathrm{a}}^{\mathrm{n}}\Delta t^{\mathrm{n}}}-1) \tag{37}$$

$$\psi^{\mathrm{n+1}} = \psi^{\mathrm{n}}-\frac{J_{\mathrm{b}}^{\mathrm{n}}\Delta t^{\mathrm{n}}}{J_{\mathrm{a}}^{\mathrm{n}}}-\frac{1-e^{J_{\mathrm{a}}^{\mathrm{n}}\Delta t^{\mathrm{n}}}}{J_{\mathrm{a}}^{\mathrm{n}}}\left(\nu^{\mathrm{n}}+\frac{J_{\mathrm{b}}^{\mathrm{n}}}{J_{\mathrm{a}}^{\mathrm{n}}}\right) \tag{38}$$

$$\Delta t^{\mathrm{n}} = \mathrm{K_t}\frac{L_{\mathrm{ref}}}{\left|\overrightarrow{v_{\mathrm{p}}^{\mathrm{G,n}}}\right|} \tag{39}$$

where, the superscripts n and n + 1 represent the time step number, Δt is the time step size, $\mathrm{K_t}$ is the time step scaling factor, L_{ref} is the reference length, i.e. the smallest grid cell dimension, and $\left|\overrightarrow{v_{\mathrm{p}}^{\mathrm{G,n}}}\right|$ is the local particle velocity magnitude. Particle-wall impingement is defined by the particle-wall distance being smaller than the particle radius. In order to avoid particle travelling into wall, a small time step size, which is determined by $\frac{0.5D_{\mathrm{p}}}{\left|\overrightarrow{v_{\mathrm{p}}^{\mathrm{G,n}}}\right|}$, is used when particle is travelling close to wall.

2.2. Non-spherical particle phase change model

The ice phase change model uses a lumped capacitance method. Therefore, ice particle temperature is assumed not to vary spatially within the particle, but does vary with time. The non-spherical shape of ice crystals is assumed to be prolate in this study (Yang et al., 2021). The phase change process is commonly assumed to consist of three stages according to the state of ice crystals, including (i) fully solid ice crystals, (ii) partially melted ice crystals, and (iii) fully melted ice crystals. During the first stage of fully solid ice crystals, the mass transfer is due to sublimation and the heat transfer is by convection and phase change. Here the particle shape remains unchanged but the particle size changes with particle mass. During the second stage, partially melted ice crystals, mass transfer is due to evaporation and the heat transfer is convection, evaporation/condensation, and melting. The particle temperature is maintained at the melting

temperature of ice. In addition, particle sphericity gradually approaches unity. Here it is assumed that fully melted particles are spherical droplets. During the third stage, fully melted ice crystals, the mass transfer is due to the evaporation/condensation and the heat transfer is from the convective and phase change heat transfer. Now the particle temperature is able to increase and the particle shape remains spherical. The effect of non-spherical particle shape on the heat and mass transfer rates is considered via the sphericity-dependent correlations of the Nusselt number, Nu, and Sherwood number, Sh, by Villedieu et al. (2014). The effect of surface blowing on the melting behaviour of ice particles is taken into account using the model of Renksizbulut and Yuen (1983), which introduces the surface blowing factor, F_{SB}, which is a function of the particle thermal properties and slip temperature between particle and gas phases. The effect of rotation on the melting behaviour of ice particles is considered using the model of Eastop (1973), here the rotation factor is introduced, F_R, which is dependent on the ratio of Re_ω to Re_p. These two factors are then used to derive the Nusselt number and Sherwood number with the effects of surface blowing and rotation (Nu^* and Sh^*) for the heat and mass equations. In addition, the ice crystal particle porosity is described using a porosity factor. The initial ice core density (ρ_{core}) is dictated by the porosity factor (PF). During the melting stage, the ice core size gradually decreases, however, its density is assumed to be unchanged.

The equations describing the three stages are listed below:

Stage 1: fully solid ice crystals → start of ice melting

$$m_p c_{p,i} \frac{dT_p}{dt} = Q_{conv} - \dot{m}_{sub} L_s \quad (40)$$

$$\frac{dm_p}{dt} = -\dot{m}_{sub} \quad (41)$$

$$Q_{conv} = \frac{\pi D_p}{\Phi} Nu^* k_g (T_f - T_p) \quad (42)$$

$$\dot{m}_{sub} = \frac{\pi D_p}{\Phi} Sh^* \rho_g D_{v,g} (\gamma_{v,p} - \gamma_{v,g}) \quad (43)$$

$$T_f = T_{g,s} \left(1 + Pr^{1/3} \frac{\gamma_f - 1}{2} Ma_{p,rel}^2 \right) \quad (44)$$

$$\rho_{core} = (1 - PF)\rho_g + PF\rho_i \quad (45)$$

$$\rho_p = \rho_{core} \quad (46)$$

where, $c_{p,i}$ is the specific heat of ice = 2108 $J/(kg.K)$, L_s is the total latent heat of fusion (L_f) and evaporation (L_v), Φ is the particle sphericity, k_g is the gas thermal conductivity, T_m is the melting temperature (273.15 K), $D_{v,g}$ is the water vapour diffusivity in the air, $\gamma_{v,p}$ and $\gamma_{v,g}$ are the vapour mass fraction at the particle surface and gas phase, respectively; $T_{g,s}$ is the local gas static temperature, Pr is the Prandtl number, γ_f is the specific heat ratio, and $Ma_{p,rel}$ is the particle Mach number based on the slip velocity. When no slip ($Ma_{p,rel} = 0$), $T_f = T_{g,s}$. The surface blowing factor, F_{SB}, which is caused by the influence of mass transfer at the particle surface on the local flowfield surrounding particles, is predicted by Renksizbulut and Yuen

(1983):

$$\mathrm{F_{SB}} = \frac{1}{\left(1+\frac{(T_{\mathrm{g,s}}-T_{\mathrm{p}})C_{\mathrm{p,p}}}{L_{\mathrm{p}}}\right)^{0.7}} \quad (47)$$

$$C_{\mathrm{p,p}} = (1-\mathrm{MR})C_{\mathrm{p,i}} + \mathrm{MR} * C_{\mathrm{p,w}} \quad (48)$$

$$L_{\mathrm{p}} = (1-\mathrm{MR})L_{\mathrm{s}} + \mathrm{MR} * L_{\mathrm{v}} \quad (49)$$

where, $C_{\mathrm{p,p}}$ and L_{p} are the specific heat and the latent heat of the ice particles, MR is the particle melt ratio. In the stage 1, the thermal properties are equal to the properties of ice; in the stage 2, mass-averaged thermal properties are used; in the stage 3, the thermal properties are equal to the properties of water. The rotation factor, $\mathrm{F_R}$, is predicted by Eastop (1973):

$$\mathrm{F_R} = \begin{cases} 1+0.167(\frac{\mathrm{Re}_\omega}{\mathrm{Re_p}}-0.54) & if \frac{\mathrm{Re}_\omega}{\mathrm{Re_p}} > 0.54 \\ 1 & if \frac{\mathrm{Re}_\omega}{\mathrm{Re_p}} \leq 0.54 \end{cases} \quad (50)$$

(51)

Therefore, the Nusselt number and Sherwood number with the effects of surface blowing and rotation, $\mathrm{Nu^*}$ and $\mathrm{Sh^*}$, are given by:

$$\frac{\mathrm{Nu^*}}{\mathrm{Nu}} = \mathrm{F_{SB}F_R} \quad (52)$$

$$\frac{\mathrm{Sh^*}}{\mathrm{Sh}} = \mathrm{F_{SB}F_R} \quad (53)$$

where, Nu and Sh are predicted by using the correlations derived by Villedieu et al. (2014):

$$\mathrm{Nu} = 2\sqrt{\varphi} + 0.55\mathrm{Pr}^{\frac{1}{3}}\varphi^{\frac{1}{4}}\sqrt{\mathrm{Re_p}} \quad (54)$$

$$\mathrm{Sh} = 2\sqrt{\varphi} + 0.55\mathrm{Sc}^{\frac{1}{3}}\varphi^{\frac{1}{4}}\sqrt{\mathrm{Re_p}} \quad (55)$$

where, Pr is the vapour Prandtl Number and Sc is the vapour Schmidt number.

Stage 2: start of ice melting $\rightarrow$ 100% liquid

$$Q_{\mathrm{conv}} = \dot{m}_{\mathrm{evap}}L_{\mathrm{v}} + \dot{m}_{\mathrm{melt}}L_{\mathrm{f}} \quad (56)$$

$$\frac{\mathrm{d}m_{\mathrm{p}}}{\mathrm{d}t} = -\dot{m}_{\mathrm{evap}} \quad (57)$$

$$\frac{\mathrm{d}m_{\mathrm{p,i}}}{\mathrm{d}t} = -\dot{m}_{\mathrm{melt}} \quad (58)$$

$$m_{\mathrm{p,w}} = m_{\mathrm{p}} - m_{\mathrm{p,i}} \quad (59)$$

$$\dot{m}_{\mathrm{evap}} = \frac{\pi D_{\mathrm{p}}}{\Phi}\mathrm{Sh^*}\rho_{\mathrm{g}}D_{\mathrm{v,g}}(\gamma_{\mathrm{v,p}} - \gamma_{\mathrm{v,g}}) \quad (60)$$

$$\rho_{\mathrm{p}} = 1/(\frac{1-\mathrm{MR}}{\rho_{\mathrm{core}}} + \frac{\mathrm{MR}}{\rho_{\mathrm{w}}}) \quad (61)$$

where, the subscripts i and w represent ice and water, respectively. Therefore, the particle melt ratio is given by:

$$\mathrm{MR} = \frac{m_{\mathrm{p,w}}}{m_{\mathrm{p}}} \quad (62)$$

Making an assumption that particle sphericity is linearly dependent on MR (Villedieu et al., 2014), particle sphericity is given by:

$$\Phi = \mathrm{MR}(1-\Phi_0)+\Phi_0 \tag{63}$$

where, Φ_0 is the initial particle sphericity.

Stage 3: 100% liquid

$$m_\mathrm{p} c_\mathrm{p,w} \frac{\mathrm{d}T_\mathrm{p}}{\mathrm{d}t} = Q_\mathrm{conv} - \dot{m}_\mathrm{evap} L_\mathrm{v} \tag{64}$$

$$\frac{\mathrm{d}m_\mathrm{p}}{\mathrm{d}t} = -\dot{m}_{evap} \tag{65}$$

$$\rho_\mathrm{p} = \rho_\mathrm{w} \tag{66}$$

2.3. Particle wall interaction model

The particle wall interaction determines the outcome of particle impingement, including rebound velocities (linear and angular velocities), shattering behaviour and sticking behaviour. In this study, the method by Villedieu et al. (2014) is used to determine the translational bounce and shattering behaviours, which divides the rebound behaviours after the particle-wall impingement into three regimes by the dimensionless parameter, ζ, representing the ratio of the normal kinetic energy to the surface energy. An additional model to predict the rebound angular velocity is employed via the method by Tsuji et al. (1985), which solves the impulsive equations and accounts for energy loss due to inelastic collision and friction. Therefore, the particle wall interaction can be shown in Fig. 2 and the equations of non-spherical particle wall interaction model are given by:

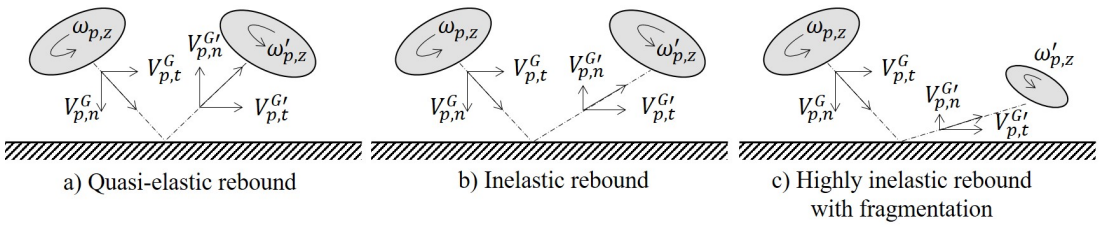

Figure 2: Configuration of the particle-wall impingement: a) Quasi-elastic rebound if $\zeta < 0.5$; b) Inelastic rebound if $\zeta \in [0.5, 90]$; c) Highly inelastic rebound with fragmentation if $\zeta > 90$.

For the translational rebound and shattering:

$$\zeta = \frac{1}{12}\frac{\rho_{\rm p} d_{\rm p} (v^{\rm G}_{\rm p,n})^2}{e_\sigma} \tag{67}$$

$$e_\sigma = e_{\sigma,0} e^{(\frac{Q_{\rm s}}{{\rm R}T_{\rm p}} - \frac{Q_{\rm s}}{{\rm R}T_0})} \tag{68}$$

$$v^{\rm G'}_{\rm p,n} = -\epsilon_{\rm n} v^{\rm G}_{\rm p,n} \tag{69}$$

$$v^{\rm G'}_{\rm p,t} = \begin{cases} \epsilon_{\rm t}(v^{\rm G}_{\rm p,t} & if \zeta < 90 \\ v^{\rm G}_{\rm p,t} + \epsilon_{\rm nt} v^{\rm G}_{\rm p,n} & if \zeta \geq 90 \end{cases} \tag{70}$$

$$\epsilon_{\rm n} = \begin{cases} 1 & if \zeta < 0.5 \\ (\frac{0.5}{\zeta})^{(1/3)} & if \zeta \geq 0.5 \end{cases} \tag{71}$$

$$\epsilon_{\rm nt} = 0.4\left(1 - \sqrt{\frac{90}{\zeta}}\right) \tag{72}$$

$$\epsilon_{\rm t} = 1 \tag{73}$$

$$d^{'}_{\rm p} = \begin{cases} \frac{d_{\rm p}}{2}(\frac{90}{\zeta})^{2/11} & if \zeta \geq 90 \\ d_{\rm p} & if \zeta < 90 \end{cases} \tag{74}$$

where, the subscripts n and t represent the velocity direction normal and tangential to wall surface, respectively; the superscript '' represents the rebound value; $e_{\sigma,0}$ is the reference surface energy =0.12 J/m^2 when T_0=253 K, $Q_{\rm s}$=4.82$\times$ 10^4 J/mol.

For the rotational rebound model:

$$C_{\rm s} = |v^{\rm G}_{\rm p,t} + \frac{D_{\rm p}}{2}\omega_{\rm p,z}| - |\frac{7}{2}{\rm C_{fs}}(1+\epsilon_{\rm n})v^{\rm G}_{\rm p,n}| \tag{75}$$

$$\omega^{'}_{\rm p,z} = \begin{cases} \frac{2}{7}\omega_{\rm p,z} - \frac{10}{7}\frac{v^{\rm G}_{\rm p,t}}{D_{\rm p}} & if {\rm C_s} \leq 0 \\ \omega_{\rm p,z} + \frac{5}{D_{\rm p}}{\rm C_{fd}}(1+\epsilon_{\rm n})v^{\rm G}_{\rm p,n} sign(v_{\rm p,t} + \frac{D_{\rm p}}{2}\omega_{\rm p,z}) & if {\rm C_s} > 0 \end{cases} \tag{76}$$

where, $\rm C_{fs}$ and $\rm C_{fd}$ are the static and dynamic coefficients of friction, = 0.05 and 0.03, receptively, for the ice impingement on steel surface (Mills, 2008).

3. Case description and set-up

3.1. Case description

A test case of a flow through a (vane-less) swan neck duct (SND) is investigated to demonstrate the rotational behaviour of non-spherical ice crystal particles. The flow domain has an inlet of width of 254 mm and height of 132 mm (Connolly et al., 2020). A schematic diagram of the test case is shown in Fig. 3. The flow conditions, which are typical of the operating conditions in the RATFac icing tunnel, are T0 = 20 $^\circ C$, P0 = 34.5 kPa, Ma = 0.4 and RH = 45%. The flow temperature in the working section of the icing tunnel gradually increases from the center to the outer region of the flow domain. Due to the lack of the temperature measurements across the working section, a uniform temperature at the inlet is used for this

simulation. The flow Reynolds number based on the inlet hydraulic diameter, Re, is approximately 5.8×10^5. Non-spherical ice crystal particles are assumed to be prolate. Particle properties investigated have diameters of 15, 40 (baseline), and 80 μm, aspect ratios of 1.5 (baseline), 2.5, and 3.5, and porosity factors of 0.6, 0.8, and 1 (baseline).

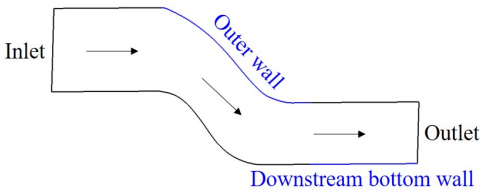

Figure 3: Schematic diagram of the flow through swan neck duct

3.2. Numerical case set-up

The gas-particle two phase flow is modelled via an Euler-Lagrange approach with one-way coupling applied.[1] The flowfield is solved in a 2D flow domain. ANSYS Fluent v19.2 is used as the aerodynamic flow solver and ICICLE is used as the solver of particle phase in the 2D domain. Steady RANS simulations are carried out to model the aerodynamic flow. The realisable κ-ϵ viscous model is used to simulate the turbulence. Scalable wall functions are used for the near wall treatment. This avoids the need to refine the boundary layer, while maintaining numerical stability in grid locations that are close to the wall. The inlet conditions are set to those described above. Further details of the boundary conditions used in the ANSYS Fluent v19.2 fluid simulation are tabulated in Appendix C. Particles are injected at the inlet with the linear and angular velocities equal those of the flow. The x-axis (the symmetry axis of the prolate) of the particles is initially aligned with the global x-axis at the inlet. The particle initial temperature is set to be 1 $^\circ C$ below the ice melting temperature. The turbulent dispersion of particles is neglected due to the high inertia of ice crystal particles in the flow domain in this study. The sub-grid scales and transient effects are neglected. The particle dimensionless numbers related to particle inertia, including the particle Stokes number, St, and particle dimensionless relaxation time, τ_p^+, are given by:

$$St = \frac{\tau_p}{\tau_\eta} \tag{77}$$

$$\tau_p^+ = \frac{\tau_p}{(\mu/\rho_\mathrm{g})/{v_*}^2} \tag{78}$$

$$\tau_p = \frac{D_\mathrm{p}^2 \rho_\mathrm{p}}{18\mu} \tag{79}$$

$$\tau_\eta = (\frac{\mu}{\rho_\mathrm{g}\epsilon})^{\frac{1}{2}} \tag{80}$$

[1]The particle volume fraction is 8.7×10^{-6} for the typical total ice content of 8 g/m^3 at the RATFac icing wind tunnel. In addition, this study focuses on studying the effect of particle tracking framework on particle trajectories and melting behaviour. Hence, two-way coupling need not be considered.

where, τ_p is the particle relaxation time, τ_η is the Kolmogorov time scale; D_p and ρ_p are the particle diameter (= 15, 40 and 80 μm) and density (= 920 kg/m^3), ρ_g is the gas density (= 0.447 kg/m^3), v_* is the mean friction velocity on the specified wall/aerofoil (= 6.6 m/s), and μ is the gas dynamic viscosity (= 1.77 $\times 10^{-5}$ kg/(m $\cdot$ s)); ϵ is the mean turbulent dissipation rate (= 6.88$\times 10^4$ m^2/s^3).

A robust numerical independence study, which is required to allow the computational accuracy and time to be balanced, is carried out at three levels considering the required resolution of (i) the mesh, (ii) the motion equation integration, and (iii) the particle count, $\mathrm{N_p}$, i.e. the number of particles injected of a specified particle size and shape. A converged value of the impingement efficiency along SND walls, IE, which can represent the severity of ice accretion, is chosen to be the criterion in the numerical independence study. The change in IE between cases is measured using mean absolute difference (MAD) of IE and these are defined by:

$$\mathrm{IE_i} = \frac{\mathrm{N_{imp,i}}}{\mathrm{N_{inlet,i}}} \tag{81}$$

$$\mathrm{MAD_X} = \left(\sum_{\mathrm{i=1}}^{\mathrm{n}} |\mathrm{IE_{i,X}} - \mathrm{IE_{i,Y}}| \right) / \mathrm{n} \tag{82}$$

where, $\mathrm{N_{imp,i}}$ is the particle count impacted on the cell surface of SND walls and $\mathrm{N_{inlet,i}}$ is the particle count injected at the inlet over an equivalent length of the cell surface; $\mathrm{IE_{i,X}}$ is the impingement efficiency at the test setting (of cell numbers, $\mathrm{K_t}$, or $\mathrm{N_p}$); $\mathrm{IE_{i,Y}}$ is the impingement efficiency at the finest setting (of cell numbers, $\mathrm{K_t}$, or $\mathrm{N_p}$) conducted in the independence study.

The grid independence study was conducted for non-spherical solid ice particles of aspect ratio 1.5 and particle size 40 μm using three 2D meshes, consisting of 0.11 million, 0.22 million and 0.32 million cells respectively. The flow solution from the mesh of 0.22 million cell mesh solution yields results close to that of 0.32 million cell mesh, as shown in Fig. 4 (a)-b) and hence is used in the remaining simulations. The MAD is seen to be 0.2% and 1.5% at the outer and downstream bottom walls, respectively. The corresponding mesh and flowfield can be found in Appendix A. An independence study of the time step scaling factor, $\mathrm{K_t}$, was carried out. As shown in Fig. 4 (c)-(d), the prediction performance by using $\mathrm{K_t} = 4$ only has a small difference compared with $\mathrm{K_t} = 1$. The MAD between these cases is 0.5% and 1.8% at the outer wall and downstream bottom wall, respectively. Therefore, $\mathrm{K_t}$ is chosen as 4, corresponding to a mean integration time step size of approximately $3 - 4 \times 10^{-6}$s. Fig. 4 (e)-(f) shows the independence study conducted for particle count, $\mathrm{N_p}$. $\mathrm{N_p}$ is chosen as 5000 as MAD is 0.4% and 0.1% at the outer and downstream bottom walls compared with $\mathrm{N_p}$=20000.

4. Results

4.1. Validation

4.1.1. Numerical validation

The developed particle tracking framework is validated against the discrete phase model (DPM) in ANSYS Fluent, which is widely used for studies of particle tracking and particle deposition. For comparison, care

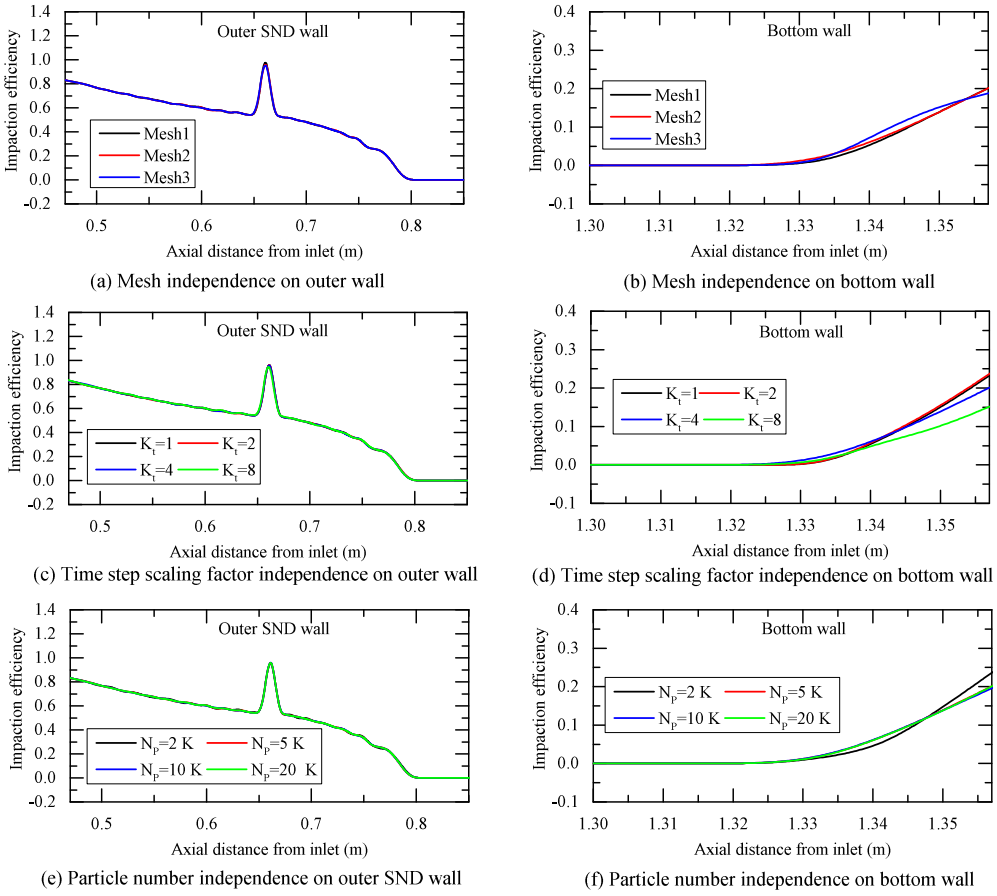

Figure 4: Mesh, time step and particle count independence study of a solid ice particle with AR=1.5 and $D_p = 40$ μm: (a)-(b) mesh independence; (c)-(d) time step independence; (e)-(f) particle count independence.

has been taken to match the numerical models and settings between the two particle tracking solvers as closely as possible. The default settings of the DPM in ANSYS Fluent are applied in order to replicate its standard implementation in the commercial code. Therefore, several adjustments have been made in ICICLE to carry out the comparison [2]. First, the ice melting model is disabled since the model is not available in the DPM. Second, spherical particles are modelled since the rotational model in DPM is only valid for spherical particles. Third, the Magnus lift force is intentionally disabled in both ICICLE and ANSYS Fluent. This is due to a defect of the implementation of Magnus lift force in ANSYS Fluent [3]. Fourth, the particle wall interaction model in ICICLE is adjusted to match the DPM model, in which the normal coefficient of restitution equals to 1 and the tangential coefficient of restitution is determined by the particle linear and angular velocities just before impingement (Ansys Inc., 2018). Particle trajectory and velocities are chosen as the comparison criteria. Fig. 5 shows the particle trajectories and velocities (linear and angular) from

[2]These adjustments are only made to enable this comparison. The results presented in other sections are predicted by the models and settings described earlier in the paper.

[3]This defect has been confirmed by ANSYS in versions up to and including "2020 R2".

simulations in ICICLE and ANSYS Fluent. It is clearly observed that the curves from ICICLE nearly overlap those from ANSYS Fluent. The mean relative differences (MRD[4]) are approximately 0.14%, 0.057%, and 1.3% for the trajectory, linear velocity, and angular velocity, respectively. As expected smaller particle more follow the gas flow, while larger particles are more ballistic, creating multiple particle-wall impingements as shown in Fig. 5 (a). Step changes in particle linear and angular velocities are observed during the particle-wall impingements as shown in Fig. 5 (b) and (c). Particles have high angular velocity post impingement, compared with their low angular velocity upstream, as show in Fig. 5 (c). After impingement, the angular velocity gradually decays due to the rotational torque - essentially, rotational drag.

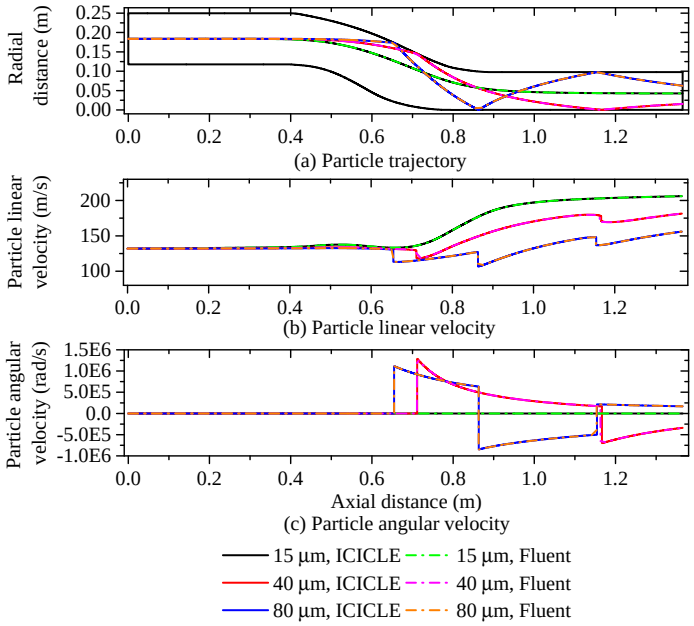

Figure 5: Comparison of the particle trajectory and velocities from simulations in ICICLE and ANSYS Fluent: (a) particle trajectory, (b) particle linear velocity, and (c) particle angular velocity.

4.1.2. Further validation against water droplet impingement test data

A water droplet impingement test performed by Papadakis et al. (2002) at NASA Glenn's Icing Research Tunnel has been selected to verify the proposed particle tracking framework since there is no equivalent impingement efficiency test available for ice crystal particles. A NACA finite swept tail aerofoil was installed in the wind tunnel of 1.8288 m height and 2.7432 m width. The freestream flow conditions were Ts = 291.2 K, Ps = 83 kPa, Ma = 0.23. The flow Reynolds number was 1.17×10^7. The water droplets had a median volume diameter (MVD) of 21 μm using 27 droplet size groups. The test case description was detailed at the first AIAA Ice Prediction Workshop (IPW Organizing Committee, 2021). The dimensionless particle

[4]MRD=MEAN(ABS(ICICLE − ANSYSFluent))/MEAN(ABS(ANSYSFluent)); MEAN is the mean value and ABS is the absolute value.

relaxation time of a 20 μm particle in this domain is approximately 1.2×10^3 and is comparable to that of a 20 μm ice crystal particle injected in the SND duct (1.3×10^3). Particle stokes number is approximately 3, 21.4 and 85.7 for 15, 40 and 80 μm particles [5]. The gas flow field was again solved using steady RANS solution in ANSYS Fluent. Water droplets, which are treated as inert spherical particles, were tracked in a 2D flow domain, with the spherical rotation model used to predict the particles' impingement behaviours. More details of the flow field, pressure distribution on the aerofoil, CFD boundary settings, and particle size distribution are given in Appendix B and Appendix C. Figure 6 shows the comparison of impingement efficiency distribution at the inboard and outboard of the aerofoil between the measurements and predictions. It can be observed that the predicted impingement efficiency distribution quantitatively matches well with the experimental measurements. The absolute difference between the predictions and measurements is within approximately 10%.

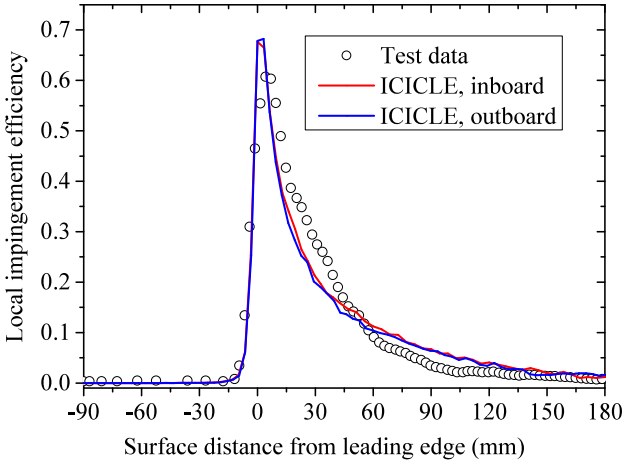

Figure 6: Comparison of impingement efficiency distribution from the test data and the predictions using ICICLE at the inboard and outboard stations of the aerofoil: the inboard and outboard stations are located at 0.9144 m and 1.1176 m above the tunnel floor.

4.2. Particle tracking method comparison

A comparison of the developed framework with other typical particle tracking methods that are used in the existing icing codes has been carried out. As shown in Table 1, three different simplified particle tracking methods (PTM 1-3), which are categorized by the methods of modelling particle motions and melting behaviours, are added and compared with the developed framework (PTM 4). More details of the methods used in PTM 1-3 can be found in Appendix F.

[5]The density of water droplets (ρ_p) is 1000 kg/m^3, the gas density (ρ_g) is 1.186 kg/m^3, the mean friction velocity on the aerofoil (v_*) is 3.67 m/s, the gas dynamic viscosity (μ) is 1.75×10^{-5} kg/(m $\cdot$ s), the mean turbulent dissipation rate (ϵ) is 2.62×10^2 m^2/s^3).

Table 1: **Details of the particle tracking methods used in the comparison.**

PTM	Models	Methods	References
1	Translational motion	Spherical drag law	Morsi and Alexander (1972)
	Rotational motion	None	
	Melting model	Spherical Nu* and Sh*	Ranz and Marshall (1952)
2	Translational motion	Non-spherical drag law	Haider and Levenspiel (1989)
	Rotational motion	None	
	Melting model	Non-spherical Nu* and Sh^*	Villedieu et al. (2014)
3	Translational motion	Spherical drag law+ lift force	Morsi and Alexander (1972) and Oesterlé and Dinh (1998)
	Rotational motion	Rotational torque	Dennis et al. (1980)
	Melting model	Spherical Nu* and Sh*; Rotation effect	Ranz and Marshall (1952) and Eastop (1973)
4	Translational motion	Non-spherical drag law+ lift force	Ouchene et al. (2016), Arcen et al. (2017) and Oesterlé and Dinh (1998)
	Rotational motion	Rotational and pitching torques	Ouchene et al. (2016) and Dennis et al. (1980)
	Melting model	Non-spherical Nu* and Sh*; Rotation effect	Villedieu et al. (2014) and Eastop (1973)

4.2.1. Single particle behaviour

Figure 7 shows the particle behaviours (trajectory, velocity and melt ratio) of the particle of 40 μm predicted by the four particle tracking methods. The deviations in the particle behaviours (trajectories and velocities) between PTM 4 and PTM 1-3 gradually become more obvious with the increase in the aspect ratio (AR). As shown in Fig. 7 (b), for PTM 4, particle gradually impacts at a farther location from the SND outlet and particle velocity gradually becomes smaller at the downstream with the increase in AR. At the SND outlet, the particle velocity reduces by approximately 6% (relative) with increasing AR from 1.5 to 2.5&3.5. However, the particle behaviours (trajectories and velocities) by PTM 2 are not obviously affected by increasing AR. The change at the outlet is smaller than 1% (relative) with increasing AR from 1.5 to 3.5. The melt ratio gradually increases with increasing AR by both PTM 2/4. At the outlet, the melt ratio increases by 4-7% and 9-14% (relative) with increasing AR from 1.5 to 2.5 and 3.5, respectively. This is attributed to the non-spherical treatment in the particle melting model in PTM 2/4 as mentioned in Table 1, which will enhance the melting potential of the non-spherical particles. In addition, PTM 4 predicts a higher melt ratio by 4-11% (relative) than PTM 2. This is due to the differences in the particle trajectories and velocities between these two methods. Fig. 8 shows the predicted $\frac{\mathrm{Re}_\omega}{\mathrm{Re}_\mathrm{p}}$ of the particles by PTM 4. $\frac{\mathrm{Re}_\omega}{\mathrm{Re}_\mathrm{p}}$

rapidly increases during the particle-wall impingements as the particle gains a high angular velocity from the impingements. However, the predicted $\frac{\mathrm{Re}_\omega}{\mathrm{Re}_\mathrm{p}}$, which is smaller than the critical value, 0.54, cannot trigger the rotation factor ($\mathrm{F_R}$) as defined by Equation (50). This indicates that the particle rotation does not directly affect the particle melting behaviour, but indirectly affect the melting behaviour through the particle trajectory and velocity in this study.

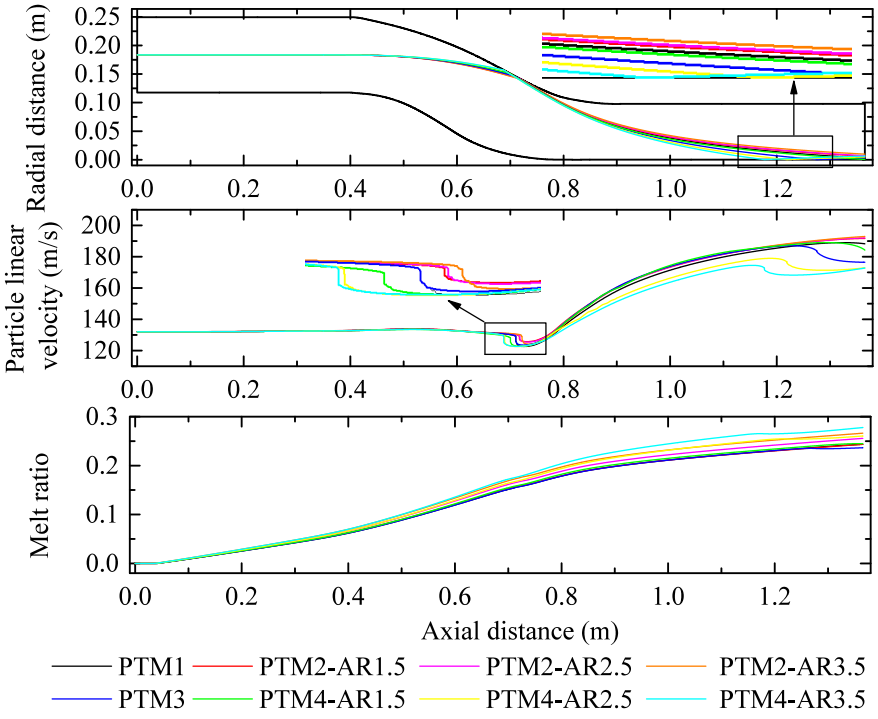

Figure 7: The predicted single particle behaviours from simulations using PTM 1-4 for $D_\mathrm{p} = 40$ μm and AR=1.5, 2.5, and 3.5.

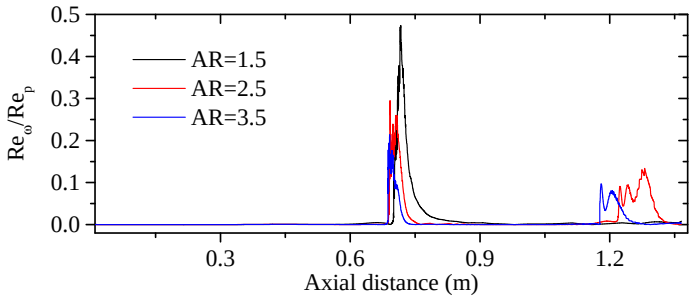

Figure 8: The predicted $\frac{\mathrm{Re}_\omega}{\mathrm{Re}_\mathrm{p}}$ from simulations using PTM 4 for $D_\mathrm{p} = 40$ μm and AR=1.5, 2.5, and 3.5.

4.2.2. Overall particle impingement behaviours

Figure 9 shows the impingement efficiency (IE) of the particles with AR=1.5 on the outer wall and downstream bottom wall using the four PTMs. As shown in Fig. 9 (a)-(c), IE generally reduces with the increase in the axial distance. PTM 4 predicts a bump of IE for 40 and 80 μm while this feature is not observed

by PTM 1-3. At the bump, IE rapidly increases to approximately 1 and then rapidly reduces. This feature is caused by the pitching torque using PTM 4. When the relatively ballistic non-spherical particles (40 and 80 μm) travel into the SND section, where the flowfield is non-uniform, the incidence angle of the particles gradually increases. This can enhance the pitching torque, which affects particle rotational and translational motion. If the pitching torque was disabled in PTM 4, the bump would disappear. Fig. 9 (d)-(e) [6] shows IE on the downstream bottom wall, which is related to the particle impingement after particles rebound from the outer wall. For 40 μm, PTM 3/4 (with rotation) predict the happening of particle impingement close to the outlet, while PTM 1/2 (without rotation) do not have particle impingement on the bottom wall. In addition, PTM 3 predicts a relatively farther impingement location from the outlet than PTM 4, as shown in Fig. 9 (d). For 80 μm, the predicted impingement locations by PTM 3/4 are farther than PTM 1/2. Also, the peak values of IE by PTM 3/4 are 25% to 75% (relative) higher than PTM 1/2. Fig. 10 shows the melt ratio of the impingement particles with AR=1.5 on the outer wall using the four PTMs. The predicted melt ratios are similar among these four PTMs. The melt ratio generally increases with the increase in the axial distance. This is due to the higher particle residence time that the particles have experienced before the particle-wall impingements. The melt ratios predicted by PTM 2/4 are slightly higher (<1%, relative) than those by PTM 1/3 and this is due to the non-spherical treatment in the particle melting model.

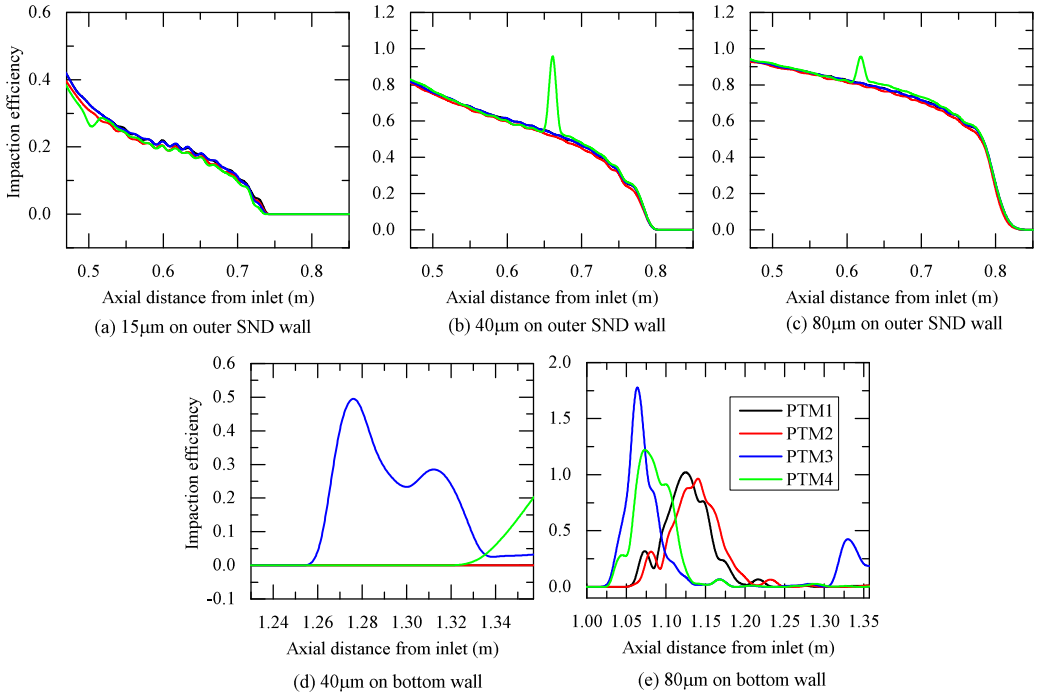

Figure 9: Comparison of the impingement efficiency of particles with AR=1.5 using PTM 1-4:(a)-(c) D_{p} = 15, 40 and 80 μm on the outer wall; (d)-(e) D_{p} = 40 and 80 μm on the downstream bottom wall.

[6]Note: The particles of 15 μm do not impact on the downstream bottom wall. Therefore, only the results of 40 and 80 μm are presented at the downstream bottom wall.

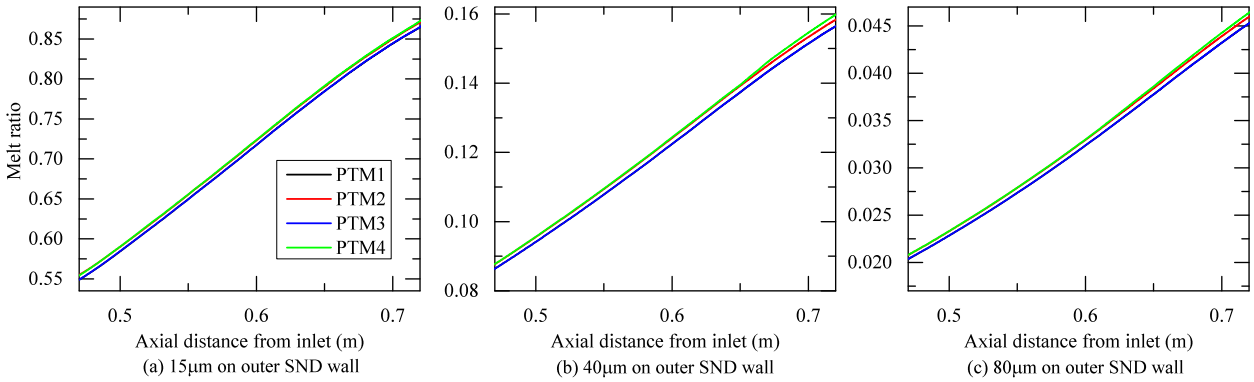

Figure 10: Comparison of the melt ratio of particles with AR=1.5 using PTM 1-4:(a-c) D_{p} = 15, 40 and 80 μm.

Figure 11 shows the effect of aspect ratio (AR) on the impingement behaviours using PTM 2 and PTM 4 for D_{p} = 40 μm. The peak value of the predicted IE by PTM 4 increases by approximately 20% (relative) with increasing AR to 2.5 and 3.5, as shown in Fig. 11 (a). In addition, the impingement location at the bottom wall gradually moves to the farther locations with increasing AR, as shown in Fig. 11 (b). However, PTM 2 is not sensitive to the change in AR as the predicted IE on the outer wall and bottom wall remains generally unchanged. The predicted melt ratio gradually increases by approximately 6% and 11% (relative) as AR is increased from 1.5 to 2.5 and 3.5 respectively. Fig. 12 shows the effect of porosity factor (PF) on the impingement behaviours [7]. Ice particles gradually become lighter and less ballistic with decreasing PF. Correspondingly, IE decreases by approximately 5-8% and 12-15% (absolute) and the melt ratio increases by approximately 24% and 62% (relative) as PF decreases to 0.8 and then 0.6.

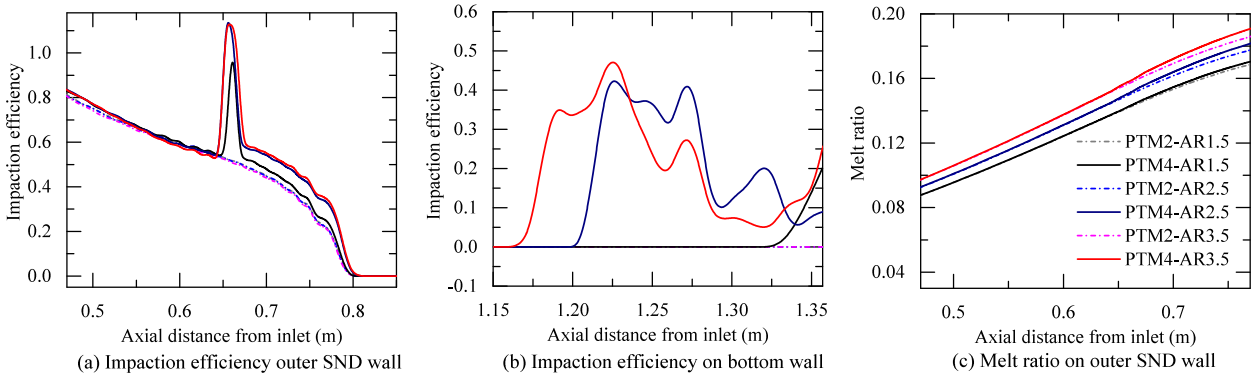

Figure 11: The effect of aspect ratio on the impingement behaviours using PTM 2 and PTM 4 for D_{p} = 40 μm and AR=1.5, 2.5, and 3.5.

[7]Note: the particle will not impact on the downstream bottom wall as PF decreases to 0.8 and 0.6. Therefore, IE on the bottom wall is not presented.

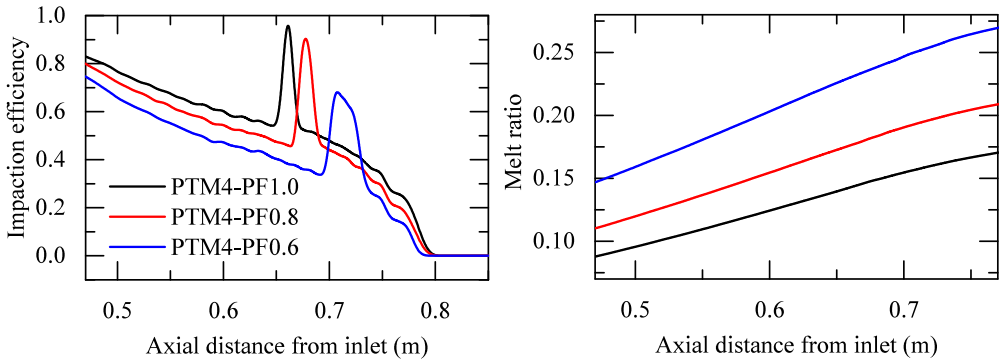

Figure 12: The effect of aspect ratio on the impingement behaviours using PTM 4 for $D_{\mathrm{p}} = 40$ μm.

4.3. Remarks on the developed particle tracking method

In this paper, a new, non-spherical particle tracking framework for ice crystal particles is developed based on non-spherical particle dynamics, particle phase change model and particle wall interaction. The trajectories and melting behaviours of ice crystal particles for the flow through the swan neck duct are predicted by the developed framework. Moreover, several existing simplified particle tracking methods are compared with the developed framework in order to understand the differences in outcome between these methods and their validity. Compared with the simplified methods, the developed framework predicts: i) a smaller particle velocity and a higher melt ratio at downstream locations for single particle's behaviour; ii) identified a "bump" feature in the impingement efficiency on the outer wall; iii) particles prefer impacting on the far downstream regions of the bottom wall from the SND outlet. These differences become larger with higher aspect ratio particles suggesting that simplified methods are insufficient to predict the particle trajectories and impingement behaviour of such particles. The results of single particle behaviour modelling show that melting is not directly affected by the particle rotation as the predicted $\frac{\mathrm{Re}_\omega}{\mathrm{Re}_\mathrm{p}}$ is smaller than the critical value. However, at real engine conditions with a highly rotational and non-uniform flowfield, the direct effect of particle rotation needs further investigation. The porosity factor of ice crystals is seen to affect both particle impingement efficiency and particle melting behaviour. With increasing porosity, particle impingement efficiency reduces and the melting potential increases.

4.3.1. Numerical uncertainty

The performance of the developed framework depends on the accuracy of the empirical correlations that are used to estimate the coefficients of forces and torques. In this study, the DNS based empirical correlations by Ouchene et al. (2016) are employed.[8] The mean relative deviations between the correlations and the DNS

[8]Note: When the particle Reynolds number is higher than 300, the force models proposed by Ouchene et al. (2016) may be not accurate enough, according to Sanjeevi et al. (2018). In this study, Re_{p} of most particles (having mean values of approximately 2.8, 24.2, and 29.6 for 15 μm, 40 μm, and 80 μm particles.) are well below 300. Hence, the force models by Ouchene et al.

data are reported to be approximately <= 10% (Ouchene et al., 2016), as shown in Fig. 13. Another set of the empirical correlations for non-spherical particle tracking, also based on DNS data, is developed by Zastawny et al. (2012). The aspect ratios of prolate considered are AR=1.25 and AR=2.5. According to Ouchene et al. (2016), the mean relative deviations of the correlations by Zastawny et al. (2012) are approximately <= 20% for drag and aerodynamic force, and <= 40% for pitching torque, as shown in Fig. 13. In order to investigate the uncertainty of the DNS-based empirical correlations, further calculations using the set of correlations developed by Zastawny et al. (2012) have been carried out for three aspect ratios (1.5, 2.0, and 2.5). The particle tracking method using the correlations by Zastawny et al. (2012) is represented by PTM 5, as shown in Table 2. Fig. 14 shows the predicted impingement efficiency and melt ratio of particles with 40 μm by both PTM 5 and PTM 4. For PTM 5, with increasing the aspect ratio, the peak values of the impingement efficiency increases and the particles melt faster. These observations are similar to PTM 4. The melt ratio by PTM 5 is close to that by PTM 4 and the differences are $< 1\%$ (relative) for all three aspect ratios. However, the location of the peak values of the impingement efficiency by PTM 5 slightly moves to a farther location from the SND outlet than PTM 4, as shown in Fig. 14 (a) and (b), especially for AR=1.5. This is attributed to the differences in the two sets of DNS correlations. As shown in Fig. 13, the differences become larger at the smaller aspect ratio, which correspondingly leads to the more obvious differences in the particle impingement efficiency for AR=1.5. Therefore, although the predicted trends in the particle behaviours between these two sets of DNS-based correlations are similar, it is suggested to employ both sets of the correlations for quantitative studies of non-spherical particle behaviours, along with a spherical particle tracking method (PTM 3) as a reference.

Table 2: **Details of the additional particle tracking method used in the comparison.**

PTM	Models	Methods	References
5	Translational motion	Non-spherical drag law+ lift force	Zastawny et al. (2012) and Oesterlé and Dinh (1998)
	Rotational motion	Rotational and pitching torques	Zastawny et al. (2012)
	Melting model	Non-spherical Nu^* and Sh^*; Rotation effect	Villedieu et al. (2014) and Eastop (1973)

(2016) is still applicable in this study. Alternatively, the force models by Zastawny et al. (2012) can be used when Re_p is larger than 300 as the model performance is still acceptable, compared to the predictions by Sanjeevi et al. (2018).

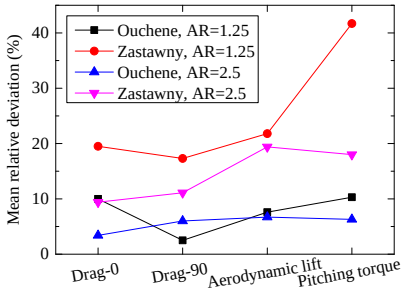

Figure 13: The mean relative deviation of the two sets of DNS correlations presented in reference (Ouchene et al., 2016): Drag-0 and Drag-90 mean the drag forces at the incidence angle of 0 and 90 °.

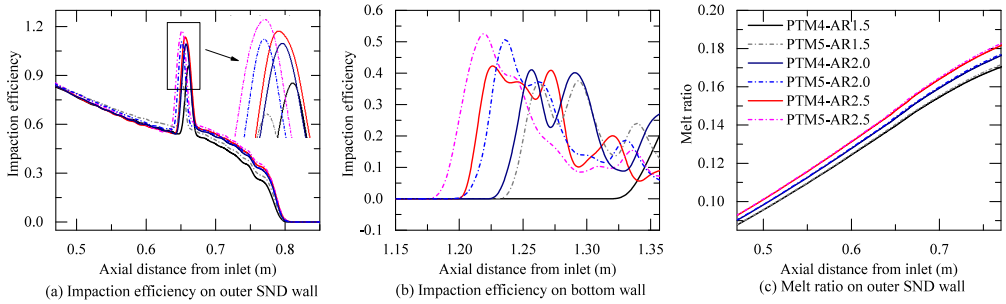

Figure 14: The particle impingement efficiency and melt ratio using PTM 4 and PTM 5 for $D_{\mathrm{p}} = 40$ μm.

4.3.2. Flow past the test body

Many existing fundamental ice crystals icing tests (Struk et al., 2011; Bucknell et al., 2019b; Currie et al., 2013, 2014; Bucknell et al., 2020) are focusing on the ice accretion due to particle impingement on a test body (wedge aerofoil, cylindrical nose, cone, stator, etc.) after particles have travelled through the working domain from an uniform upstream flowfield. This is different from the non-uniform flowfield of the swan neck duct in this study. Therefore, further calculations of a flow past a test body (cone and stator) have been undertaken. More details of the flowfield of the cone and stator cases can be found in Appendix E. Fig. 15 shows the impingement efficiency of particles with AR=1.5 on the test bodies of cone and stator using PTM 1-5. The predicted IE for all five PTMs are similar and especially amongst PTM 1-4. The difference is within 1% (absolute) for 40 and 80 μm particles and slightly increases to approximately 3% (absolute) for 15 μm particles. Small differences are associated with a well conditioned uniform upstream flowfield. This results in very limited particle rotation behaviour, which has minimal effect of the particle impingement efficiency on the test bodies (stator and cone). Fig. 16 shows the melt ratio of the impingement particles on the test bodies of cone and stator using PTM 1-5. The melt ratios predicted by PTM 2/4/5 are approximately 2% (relative) higher than those by PTM 1/3. This is attributed to the non-spherical treatment in the melting models in PTM 2/4/5. These observations suggest that the simplified particle tracking methods could be acceptable for predicting the impingement behaviours for this kind of scenario, at least for the prolate particles of the

aspect ratio range investigated in this study.

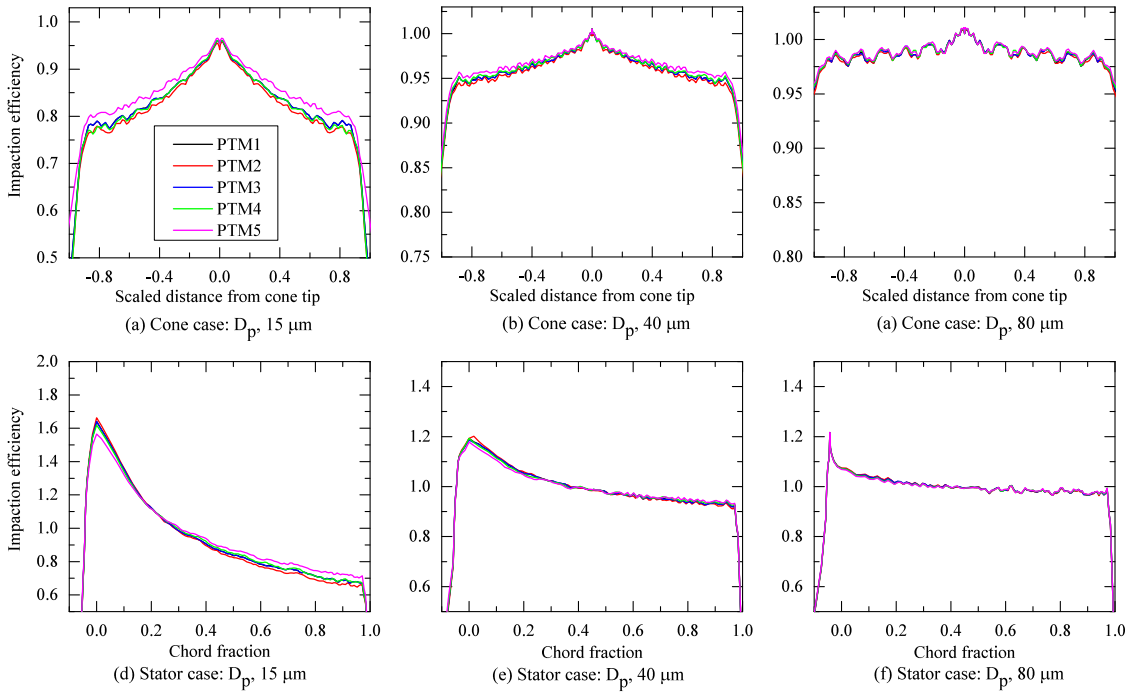

Figure 15: The impingement efficiency of particles with AR=1.5 from simulations of the cone and stator case using PTM 1-5 for $D_{\mathrm{p}} = 15$, 40 and 80 μm.

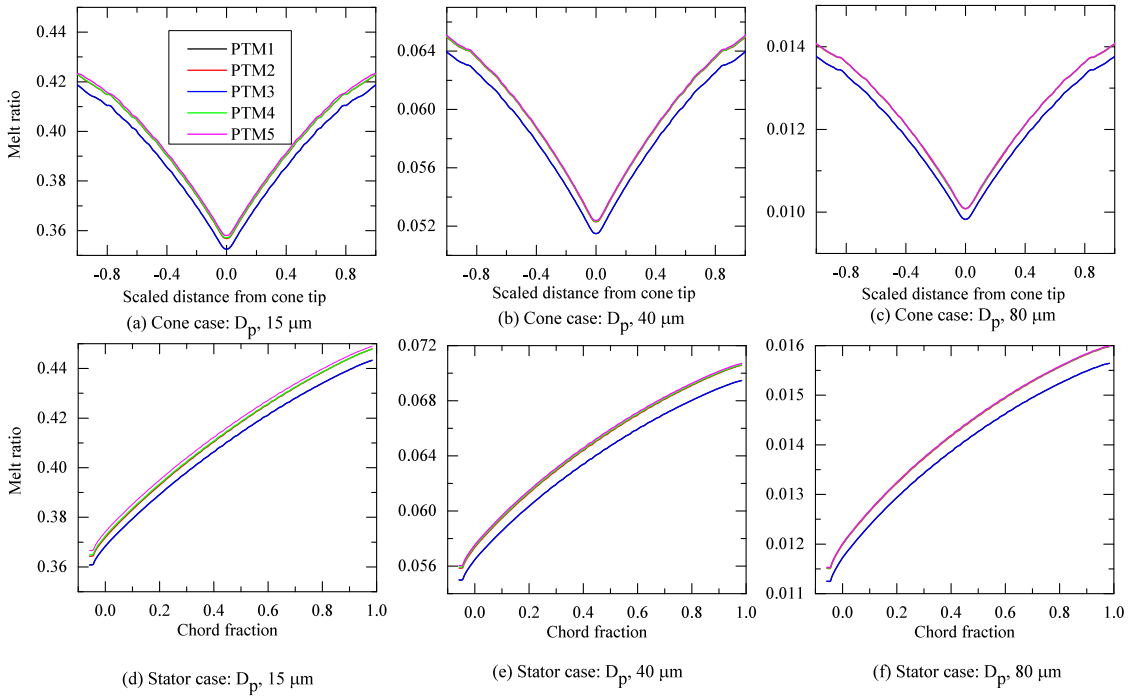

Figure 16: The melt ratio of particles with AR=1.5 from simulations of the cone and stator case using PTM 1-5 for $D_{\mathrm{p}} = 15$, 40 and 80 μm.

5. Conclusions

A 2D framework has been developed to model the particle trajectory and melting behaviour for non-spherical ice crystal particles. A test case of flow through a swan neck duct is investigated. Discrete functional capabilities of the developed framework are validated against the well-known discrete phase model in ANSYS Fluent and an experimental water droplet impingement test for tracking rotating spherical particles. Nearly identical particle trajectories and velocities are observed when appropriately matched boundary conditions are applied. Also, the ICICLE predictions agree well with the water droplet impingement test data. The main conclusions are:

1. Obvious deviations in individual particles' behaviours (trajectory, velocity and melt ratio) and overall particle impingement behaviour (impingement efficiency) are observed between the developed framework and simplified particle tracking methods. The deviations become larger when higher aspect ratio particles are modelled. At the SND outlet, the particle velocity drops by approximately 6% (relative) and melt ratio increases by 4-7% and 9-14% (relative) as the prolate AR in increased from 1.5 to 2.5/3.5. The implication here is that existing simplified methods may be insufficient to predict non-spherical ice crystal behaviours. However, for the flow past a test body with an uniform upstream flowfield, the differences in the particle impingement behaviours between the developed framework and the simplified methods are relatively small within 1-3 % (absolute) difference of impingement efficiency. Thus validation with existing typical test cases using simplified particle tracking methods and a non-spherical particle melting model may appear sufficient, yet still be unreliable for real engine geometries. Therefore, in order to better understand particle trajectory and melting behaviour, it is suggested to employ the non-spherical particle tracking method with rotation, along with the spherical particle tracking method as a reference.
2. Larger aspect ratio particles have a higher melting potential. Also, the aspect ratio was seen to increase the particle impingement efficiency for the swan neck duct case. The peak IE of the 40 μm particle increases by approximately 20% (relative) as AR is increased from 1.5 to 2.5/3.5. Larger particle porosity reduces particle impingement efficiency and increases particle melting potential. IE decreases by 12-15% (absolute) and the melt ratio increases by approximately 62% (relative) with decreasing the porosity factor from 1 to 0.6. This highlights the importance to experimentally determining the porosity of ice crystal particles entering the flow domain for modelling ICI.
3. The numerical uncertainty is studied via consideration of two sets of DNS-derived correlations of forces and torques. The predicted trends in the particle behaviours between these two sets of DNS-based correlations are similar. However, the predicted particle impingement locations are different on the downstream bottom wall, especially for smaller aspect ratio particles.

Acknowledgments

The authors would like to acknowledge Rolls-Royce and the Aerospace Technology Institute (ATI) for funding provided within their De-ICER programme which supported this research.

Appendix A. SND Mesh and velocity contour

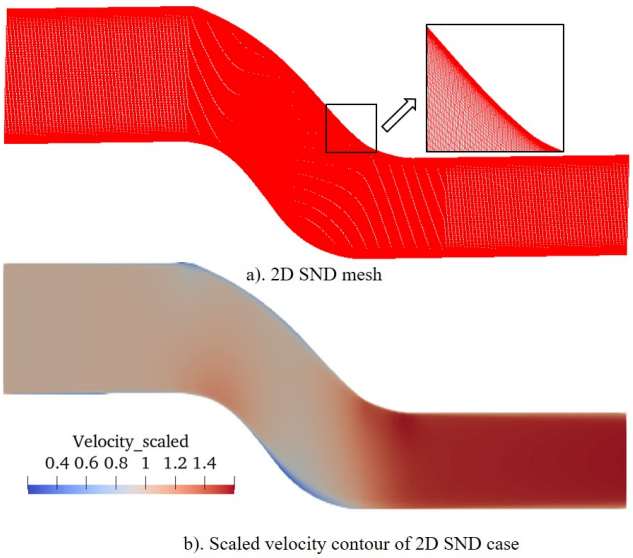

Figure A.17: Mesh and velocity contour used to simulate particle behaviours of the SND case (not to scale): a) Mesh; b) Scaled velocity contour.

Appendix B. Velocity contour and pressure distribution of the NASA case

Figure B.18: Velocity contour (domain dimension not to scale) at the inboard plane of the NASA finite swept tail case.

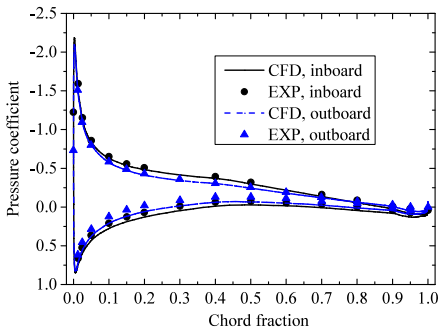

Figure B.19: Comparison of pressure distribution at the inboard and outboard of NASA finite swept tail case.

Appendix C. Boundary conditions used in ANSYS Fluent and particle size distribution

Table C.3: Boundary conditions used in ANSYS Fluent.

		Inlet				Outlet	
	Ps_{opt}, kPa	V, m/s	Ts, K	I_{turb}	D_h, m	P_{gauge}, kPa	Wall
SND	30.9	132	284.1	5%	0.174	0	No slip adiabatic wall
NASA	83.0	78.7	291.2	5%	2.195	0	No slip adiabatic wall

where, Ps_{opt} is the operating static pressure, I_{turb} is the turbulence intensity, and P_{gauge} is the gauge pressure.

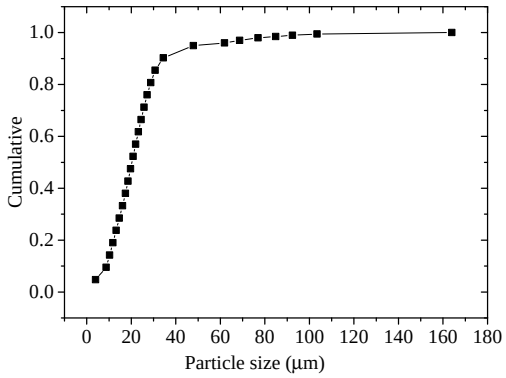

Figure C.20: Cumulative particle size distribution of the NASA water droplet impingement test (MVD = 21μm).

Appendix D. Flow and particle characteristic properties

where, the mean Re_p of the SND case is for ice particles of aspect ratio=1.5 and porosity factor=1.

Table D.4: Flow Reynolds number and Kolmogorov time scale.

	SND	NASA
Re	5.8×10^5	1.17×10^7
τ_η, s	2.4×10^{-5}	2.37×10^{-4}

Table D.5: Particle characteristic properties.

	SND			NASA		
	15μm	40μm	80μm	15μm	40μm	80μm
τ_p, s	6.5×10^{-4}	4.62×10^{-3}	1.85×10^{-2}	7.14×10^{-4}	5.08×10^{-3}	2.03×10^{-2}
St	27.1	192.6	770.3	3.0	21.4	85.7
τ_p^+	7.15×10^2	5.08×10^3	2.03×10^4	6.52×10^2	4.64×10^3	1.85×10^4
Mean Re_p	2.8	24.2	29.6	0.75	4.2	14.2

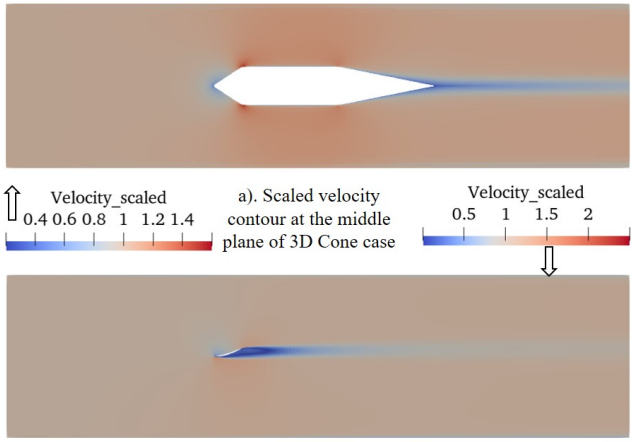

Figure E.21: Scaled velocity contour (domain dimension not to scale): a) Middle plane of 3D Cone case; b) Middle plane of 3D Stator case.

Appendix E. Velocity contour of the cone and stator cases

Appendix F. Additional equations

Additional equations that are used in PTM 1-3 and PTM 5 are presented in this section.

The spherical drag law by is given by:

$$\mathrm{C_D} = \mathrm{a_1} + \frac{\mathrm{a_2}}{\mathrm{Re_p}} + \frac{\mathrm{a_3}}{\mathrm{Re_p^2}} \tag{A.1}$$

where, $\mathrm{a_1}$, $\mathrm{a_2}$ and $\mathrm{a_3}$ are constants that are given by Morsi and Alexander (1972).

The non-spherical drag law is given by Haider and Levenspiel (1989):

$$C_D = \frac{24}{Re_p}\left(1 + b_1 Re_p^{b_2}\right) + \frac{b_3 Re_p}{b_4 + Re_p} \tag{A.2}$$

$$b_1 = \exp(2.3288 - 6.4581\Phi + 2.4486\Phi^2) \tag{A.3}$$

$$b_2 = 0.0964 + 0.5565\Phi \tag{A.4}$$

$$b_3 = \exp(4.905 - 13.8944\Phi + 18.42226\Phi^2 - 10.2599\Phi^3) \tag{A.5}$$

$$b_4 = \exp(1.4681 + 12.2584\Phi - 20.7322\Phi^2 + 15.8855\Phi^3) \tag{A.6}$$

A linear interpolation of the correlation of drag, lift and torques by Zastawny et al. (2012) is employed and the formula is given by:

$$C_{D,AR} = \frac{1}{1.25}\left[(C_{D,2.5} - C_{D,1.25})AR + (2.5C_{D,1.25} - 1.25C_{D,2.5})\right] \tag{A.7}$$

$$C_{la,AR} = \frac{1}{1.25}\left[(C_{la,2.5} - C_{la,1.25})AR + (2.5C_{la,1.25} - 1.25C_{la,2.5})\right] \tag{A.8}$$

$$C_{TP,AR} = \frac{1}{1.25}\left[(C_{TP,2.5} - C_{TP,1.25})AR + (2.5C_{TP,1.25} - 1.25C_{TP,2.5})\right] \tag{A.9}$$

$$C_{TR,AR} = \frac{1}{1.25}\left[(C_{TR,2.5} - C_{TR,1.25})AR + (2.5C_{TR,1.25} - 1.25C_{TR,2.5})\right] \tag{A.10}$$

$$\tag{A.11}$$

where, C_D, C_{la},C_{TP}, and C_{TR} at AR= 1.25 or 2.5 are given by:

$$C_D = C_{D,0} + (C_{D,\pi/2} - C_{D,0})\sin^{a_0}(\varphi) \tag{A.12}$$

$$C_{D,0} = \frac{a_1}{Re_p^{a_2}} + \frac{a_3}{Re_p^{a_4}} \tag{A.13}$$

$$C_{D,\pi/2} = \frac{a_5}{Re_p^{a_6}} + \frac{a_7}{Re_p^{a_8}} \tag{A.14}$$

$$C_{la} = \left(\frac{b_1}{Re_p^{b_2}} + b_3 Re_p^{b_4}\right)\sin^{b_5 + b_6 Re_p^{b_7}}(\varphi)\cos^{b_8 + b_9 Re_p^{b_{10}}}(\varphi) \tag{A.15}$$

$$C_{TP} = \left(\frac{c_1}{Re_p^{c_2}} + c_3 Re_p^{c_4}\right)\sin^{c_5 + c_6 Re_p^{c_7}}(\varphi)\cos^{c_8 + c_9 Re_p^{c_{10}}}(\varphi) \tag{A.16}$$

$$C_{TR} = r_1 Re_\omega^{r_2} + \frac{r_3}{Re_\omega^{r_4}} \tag{A.17}$$

where, a_0-a_8, b_1-b_{10}, c_1-c_{10}, and r_1-r_4 are constants that are given by Zastawny et al. (2012).

Spherical Nu^* and Sh^* are given by Ranz and Marshall (1952):

$$Nu^* = 2 + 0.6 Re_p^{\frac{1}{2}} Pr^{\frac{1}{3}} \tag{A.18}$$

$$Sh^* = 2 + 0.6 Re_p^{\frac{1}{2}} Sc^{\frac{1}{3}} \tag{A.19}$$

References

Ansys Inc., 2018. ANSYS FLUENT 19.2 Theory Guide. Ansys Inc.

Arcen, B., Ouchene, R., Khalij, M., Tanière, A., 2017. Prolate spheroidal particles' behavior in a vertical wall-bounded turbulent flow. Physics of Fluids 29, 093301. doi:10.1063/1.4994664.

Ayan, E., Özgen, S., 2018. In-flight ice accretion simulation in mixed-phase conditions. The Aeronautical Journal 122, 409–441. doi:10.1017/aer.2017.127.

Bucknell, A., McGilvray, M., Gillespie, D., Jones, G., Collier, B., 2019a. A three-layer thermodynamic model for ice crystal accretion on warm surfaces: EMM-C, in: International Conference on Icing of Aircraft, Engines, and Structures, SAE Paper 2019-01-1963. doi:10.4271/2019-01-1963.

Bucknell, A., McGilvray, M., Gillespie, D., Parker, L., Forsyth, P., Saad Ifti, H., Jones, G., Collier, B., Reed, A., 2019b. Experimental study and analysis of ice crystal accretion on a gas turbine compressor stator vane, in: International Conference on Icing of Aircraft, Engines, and Structures, SAE Paper 2019-01-1927. doi:10.4271/2019-01-1927.

Bucknell, A., McGilvray, M., Gillespie, D., Yang, X., Jones, G., Collier, B., 2019c. Icicle: A model for glaciated & mixed phase icing for application to aircraft engines, in: International Conference on Icing of Aircraft, Engines, and Structures, SAE Paper 2019-01-1969. doi:10.4271/2019-01-1969.

Bucknell, A., McGilvray, M., Gillespie, D.R.H., Jones, G., Reed, A., Collier, B., 2020. Experimental studies of ice crystal accretion on axisymmetric bodies at aeroengine conditions. Journal of Propulsion and Power 36, 836–850. doi:10.2514/1.B37635.

Connolly, J., Choi, M., Yang, X., Doherty, L.J., McGilvray, M., Gillespie, D.R., Collier, B., Jones, G., 2020. Ice crystal accretion in a combined linear cascade and swan neck duct, in: AIAA AVIATION 2020 FORUM, AIAA Paper 2020-2828. doi:10.2514/6.2020-2828.

Currie, T.C., Fuleki, D., Knezevici, D.C., MacLeod, J.D., 2013. Altitude scaling of ice crystal accretion, in: 5th AIAA Atmospheric and Space Environments Conference, AIAA Paper 2013-2677. doi:10.2514/6.2013-2677.

Currie, T.C., Fuleki, D., Mahallati, A., 2014. Experimental studies of mixed-phase sticking efficiency for ice crystal accretion in jet engines, in: 6th AIAA Atmospheric and Space Environments Conference, AIAA Paper 2014-3049. doi:10.2514/6.2014-3049.

Dennis, S., Singh, S., Ingham, D., 1980. The steady flow due to a rotating sphere at low and moderate reynolds numbers. Journal of Fluid Mechanics 101, 257–279. doi:10.1017/S0022112080001656.

Eastop, T., 1973. The influence of rotation on the heat transfer from a sphere to an air stream. International Journal of Heat and Mass Transfer 16, 1954–1957. doi:10.1016/0017-9310(73)90215-9.

Haider, A., Levenspiel, O., 1989. Drag coefficient and terminal velocity of spherical and nonspherical particles. Powder Technology 58, 63–70. doi:10.1016/0032-5910(89)80008-7.

Hölzer, A., Sommerfeld, M., 2008. New simple correlation formula for the drag coefficient of non-spherical particles. Powder Technology 184, 361–365. doi:10.1016/j.powtec.2007.08.021.

IPW Organizing Committee, 2021. Ice prediction workshop test case descriptions. https://folk.ntnu.no/richahan/IPW/. Accessed: 2021-07-06.

Mason, J., Strapp, W., Chow, P., 2006. The ice particle threat to engines in flight, in: 44th AIAA Aerospace Sciences Meeting and Exhibit, AIAA Paper 2006-206. doi:10.2514/6.2006-206.

Mason, J.G., Chow, P., Fuleki, D.M., 2011. Understanding ice crystal accretion and shedding phenomenon in jet engines using a rig test. Journal of Engineering for Gas Turbines and Power 133, 041201. doi:10.1115/1.4002020.

Mills, A., 2008. The coefficient of friction, particularly of ice. Physics Education 43, 392–395. doi:10.1088/0031-9120/43/4/006.

Morsi, S.A., Alexander, A.J., 1972. An investigation of particle trajectories in two-phase flow systems. Journal of Fluid Mechanics 55, 193–208. doi:10.1017/S0022112072001806.

Nilamdeen, S., Rao, V.S., Switchenko, D., Selvanayagam, J., Ozcer, I., Baruzzi, G.S., 2019. Numerical simulation of ice crystal accretion inside an engine core stator, in: International Conference on Icing of Aircraft, Engines, and Structures, SAE Paper 2019-01-2017. doi:10.4271/2019-01-2017.

Norde, E., Senoner, J.M., van der Weide, E.T.A., Trontin, P., Hoeijmakers, H.W.M., Villedieu, P., 2019. Eulerian and lagrangian ice-crystal trajectory simulations in a generic turbofan compressor. Journal of Propulsion and Power 35, 26–40. doi:10.2514/1.B36916.

Norde, E., van der Weide, E.T.A., Hoeijmakers, H.W.M., 2017. Eulerian method for ice crystal icing. AIAA Journal 56, 222–234. doi:10.2514/1.J056184.

Oesterlé, B., Dinh, T.B., 1998. Experiments on the lift of a spinning sphere in a range of intermediate reynolds numbers. Experiments in Fluids 25, 16–22. doi:10.1007/s003480050203.

Ouchene, R., Khalij, M., Arcen, B., Tanière, A., 2016. A new set of correlations of drag, lift and torque coefficients for non-spherical particles and large reynolds numbers. Powder Technology 303, 33–43. doi:10.1016/j.powtec.2016.07.067.

Palmer, R., Roberts, I., Moser, R., Hatch, C., Smith, F., 2019. Non-spherical particle trajectory modelling for ice crystal conditions, in: International Conference on Icing of Aircraft, Engines, and Structures, SAE Paper 2019-01-1961. doi:10.4271/2019-01-1961.

Papadakis, M., Hung, K.E., Vu, G.T., Yeong, H.W., Bidwell, C.S., Breer, M.D., Bencic, T.J., 2002. Experimental investigation of water droplet impingement on airfoils, finite wings, and an s-duct engine inlet, NASA/TM-2002-211700.

Ranz, W., Marshall, W.R., 1952. Evaporation from drops. Chem. eng. prog 48, 141–146.

Renksizbulut, M., Yuen, M.C., 1983. Experimental Study of Droplet Evaporation in a High-Temperature Air Stream. Journal of Heat Transfer 105, 384–388. doi:10.1115/1.3245590.

Sanjeevi, S.K., Kuipers, J., Padding, J.T., 2018. Drag, lift and torque correlations for non-spherical particles from stokes limit to high reynolds numbers. International Journal of Multiphase Flow 106, 325–337. doi:https://doi.org/10.1016/j.ijmultiphaseflow.2018.05.011.

Struk, P., Currie, T., Wright, W.B., Knezevici, D.C., Fuleki, D., Broeren, A., Vargas, M., Tsao, J.C., 2011. Fundamental ice crystal accretion physics studies, in: SAE 2011 International Conference on Aircraft and Engine Icing and Ground Deicing, SAE Paper 2011-38-0018.

Trontin, P., Villedieu, P., 2018. A comprehensive accretion model for glaciated icing conditions. International Journal of Multiphase Flow 108, 105–123. doi:10.1016/j.ijmultiphaseflow.2018.06.023.

Tsuji, Y., Oshima, T., Morikawa, Y., 1985. Numerical simulation of pneumatic conveying in a horizontal pipe. KONA Powder and Particle Journal 3, 38–51. doi:10.14356/kona.1985009.

Villedieu, P., Trontin, P., Chauvin, R., 2014. Glaciated and mixed phase ice accretion modeling using onera 2d icing suite, in: 6th AIAA Atmospheric and Space Environments Conference, AIAA Paper 2014-2199.

van Wachem, B., Zastawny, M., Zhao, F., Mallouppas, G., 2015. Modelling of gas–solid turbulent channel flow with non-spherical particles with large stokes numbers. International Journal of Multiphase Flow 68, 80–92. doi:10.1016/j.ijmultiphaseflow.2014.10.006.

Widhalm, M., 2015. Lagrangian trajectory simulation of rotating regular shaped ice particles, in: SAE 2015 International Conference on Icing of Aircraft, Engines, and Structures, SAE Paper 2015-01-2141. doi:10.4271/2015-01-2141.

Wright, W., Jorgenson, P., Veres, J., 2010. Mixed phase modeling in glennice with application to engine icing, in: AIAA Atmospheric and Space Environments Conference, AIAA Paper 2010-7674. doi:10.2514/6.2010-7674.

Wright, W.B., Struk, P., Bartkus, T., Addy, G., 2015. Recent advances in the lewice icing model, SAE Paper 2015-01-2094. doi:10.4271/2015-01-2094.

Yang, X., McGilvray, M., Gillespie, D., 2021. Numerical modelling and parametric study of the melting behaviour of ice crystal particles. AIAA Journal doi:10.2514/1.J060351.

Zastawny, M., Mallouppas, G., Zhao, F., van Wachem, B., 2012. Derivation of drag and lift force and torque coefficients for non-spherical particles in flows. International Journal of Multiphase Flow 39, 227–239. doi:10.1016/j.ijmultiphaseflow.2011.09.004.